Submitted to Colloids and Surfaces A: Physicochemical and Engineering Aspects
for the special issue honouring Prof. Ivan B. Ivanov, Faculty of Chemistry, Sofia University

Foam-wall friction: Effect of air volume fraction for tangentially immobile bubble surface

Nikolai D. Denkov,*[1] Slavka Tcholakova,[1] Konstantin Golemanov,[1]
Vivek Subramanian,[2] and Alex Lips[2]

[1]*Laboratory of Chemical Physics & Engineering, 1 James Bourchier Ave., 1164 Sofia, Bulgaria*

[2]*Unilever Global Research Center, Trumbull, Connecticut 06611, USA*

*Corresponding author:
Assoc. Prof. Nikolai D. Denkov
Laboratory of Chemical Physics & Engineering
Faculty of Chemistry, Sofia University
1 James Bourchier Ave., 1164 Sofia
Bulgaria

Phone: (+359-2) 962 5310
Fax: (+359-2) 962 5643
E-mail: ND@LCPE.UNI-SOFIA.BG

Keywords: foam rheology, wall slip, viscous friction in foams, bubble-wall friction, Bretherton problem.

ABSTRACT

Wall-slip is an important phenomenon for the rheological behavior of various dispersions, including foams. In a previous study [Denkov et al., Colloids & Surfaces A 263 (2005) 129] we showed experimentally that the viscous stress between a foam and sliding solid wall is proportional to $Ca^{1/2}$ for a foam generated from potassium carboxylate surfactants at air volume fraction of Φ_{3D} = 90 % ($Ca = \mu V_0/\sigma$ is the capillary number). This experimental finding was explained by a theoretical model, whose main assumptions were: (1) the foam bubbles had tangentially immobile surface, and (2) the viscous friction occurred only in the dynamic wetting films formed between the bubbles and the solid wall. The current study is a continuation of our previous work, with the major aim to clarify theoretically the effect of air volume fraction, Φ, on the foam-wall friction (the variation of Φ is equivalent to varying the ratio of the film to Plateau border radii, R_F/R_P). By using the lubrication approximation, we show with numerical calculations that for bubbles with tangentially immobile surfaces, more generally, the bubble-wall friction force could be represented as a superposition of two components: friction inside the wetting film, which is proportional to $Ca^{1/2}$ and friction in the transition zone film-meniscus, which is proportional to ($A_1Ca^{3/4} - A_2Ca$), where $A_{1,2}$ are numerical constants depending on Φ. The numerical calculations show also that the term describing the friction in the transition zone film-meniscus, is very well approximated by $A_3Ca^{2/3}$ in the range of capillary numbers $10^{-6} \leq Ca \leq 10^{-3}$. An explicit expression is proposed, which describes rather well the numerical results for the friction force. The calculations show that the relative contribution of the friction inside the film dominates at $\Phi_{3D} \geq$ ca. 90 %. However, at lower air volume fractions (i.e. at smaller ratio R_F/R_P) the friction in the transition zone film-meniscus could be significant and the effective power law index could have a value close to 2/3, as predicted in Bretherton's model [F.P. Bretherton, J. Fluid Mech. 10 (1961) 166]. The predictions of the current model are verified with literature data about the bubble-wall friction force, as well as with original experimental results about the thickness of the dynamic wetting films, formed between bubbles and moving solid wall. The obtained results could be useful in the analysis of the particle-wall friction in other systems, such as emulsions and dispersions of gel particles. The theoretical approach could be modified to describe various phenomena, such as motion of drops/bubbles in capillaries (including microfluidic applications) and hydrodynamic lubrication of deformable solid particles.

1. Introduction.

The foam-wall friction is an important phenomenon, which should be taken into account when considering the foam flow and the rheological measurements of foams [1-11]. This friction occurs in the contact zones of the foam bubbles with the solid wall, and from physico-chemical viewpoint it is related to other phenomena, which have recently attracted a considerable interest in several research areas: emulsion-wall friction in relation to emulsion rheology [3-5,12], wall-slip in dispersions of gel particles or vesicles [13-15], and motion of bubbles, drops and other deformable particles (vesicles, biological cells) in narrow capillaries [1,7,16-26], including the recent activity in microfluidics [27-31]. The common feature of all these systems is the formation of a dynamic film between the deformable particles and the solid wall. The thickness of this dynamic film depends on the relative velocity of the particle and the wall, which has important consequences for the particle-wall friction.

Experimental and theoretical studies [1,7,9,11,16-23] showed for foams, emulsions, and bubbles in narrow capillaries that various properties, such as the viscous stress created by the particle-wall friction and the average thickness of the dynamic films are well represented by power-law functions of the capillary number, $Ca = \mu V_0/\sigma$, where μ is the fluid viscosity, V_0 is the relative velocity of the particle and the wall, and σ is the interfacial tension. However, a significant uncertainty still exists in the literature on the reasons why different power-law indexes, n, are measured in various experiments, and moreover, why the experimental results are often in an apparent contradiction with the available theoretical models. From this viewpoint, further experimental and theoretical efforts, aimed to reveal the relations between the various systems and to reconcile the theoretical predictions with the experimental results, seem well justified.

In our previous study [11] we showed experimentally and theoretically that the viscous stress between sheared foam and solid wall could be proportional to $Ca^{1/2}$ or $Ca^{2/3}$, depending on the used surfactant. In the first case, the viscous dissipation occurs mainly inside the wetting films formed between the bubbles and the solid wall. Experimentally, this case was realized by using a mixture of potassium carboxylates with relatively long hydrocarbon chains (12 to 18 carbon atoms) as surfactants, and foams with air volume fraction, $\Phi_{3D} = 90$ %. In the second case, analysed originally by Bretherton [18] and studied numerically in detail by Saugey et al. [9], the viscous friction occurs mainly in the transition zone between the wetting film and the Plateau border region around the film, which is a typical case for synthetic surfactants, which render tangential mobility of the bubble surface. This behavior was observed with foams stabilized by sodium dodecyl sulfate (SDS), cocoamidopropyl betaine (Betaine), and other surfactants [11].

The current study is a continuation of our previous work [11], with a major aim to describe theoretically the effect of air volume fraction, Φ, on the viscous friction between bubbles with tangentially immobile surfaces and solid wall. We take into account the fact that the viscous friction in the real systems occurs simultaneously in the two zones mentioned

above, namely, inside the wetting film and in the transition zone film-meniscus. The volume fraction, Φ, controls the relative size of the wetting films between the bubbles and the wall, viz., the ratio R_F/R_P, where R_F is the film radius and R_P is the radius of curvature of the Plateau border. Thus, Φ is one of the key parameters controlling the relative contributions of the two friction zones into the total friction force.

The theoretical analysis and the numerical calculations performed in the current study show that the bubble-wall viscous friction depends primarily on two types of factors: (1) geometrical, which include the bubble size, R_0, and the ratio R_F/R_P; (2) dynamic, which are accounted for by the capillary number, Ca. Simple explicit expression for the total friction force is constructed, which describes the numerical results from the model calculations as a superposition of the viscous stresses inside the aforementioned two friction regions. The results show that the contributions originating from the two friction zones have different power-law dependences on the capillary number, Ca, which are similar to those considered separately in the previous studies [11,18]. At high air volume fractions, the friction inside the film dominates and the friction force is proportional to $Ca^{1/2}$, whereas at lower volume fractions the friction stresses originating from the film and meniscus regions are comparable. Therefore, the current model predicts different power-law indexes, depending on the values of Φ and Ca, and the conditions for the transition from film-dominated to mixed friction regime are clarified. The theoretical predictions for the thickness of the dynamic wetting film between a bubble and a moving wall are compared with original experimental results (determined by optical microscopy in reflected light) and a very good agreement is found.

The paper is structured as follows: In Section 2 we describe the theoretical model. In Section 3 we present the numerical results. In Section 4 we show how the foam-wall viscous stress could be calculated from the friction force between a single bubble and a wall. Section 5 describes the experimental procedure used to measure the film thickness and the comparison of theory and experiment. Section 6 contains a brief discussion of the results and their relation to previous studies by other authors. Section 7 summarizes the conclusions.

2. Theoretical model.

2.1. System under consideration

Following our previous study [11], we consider first the viscous friction between an infinitely-long cylindrical 2D-bubble and a wall, with the bubble axis being parallel to the wall surface. The coordinate system is fixed to the bubble, which is thus considered as immobile. The velocity of the solid substrate, V_0, is directed along the x-axis, which is perpendicular to the axis of the 2D-bubble, see Fig. 1. The radius of the wetting film is denoted with R_F, whereas the profile of the meniscus regions unperturbed by the viscous friction, is represented by circular arcs with radius R_P, see Fig. 1.

In static system (immobile solid wall), the scaled film and Plateau-border radii, R_F/R_0 and R_P/R_0, are functions of the air volume fraction only, Φ, where R_0 is the radius of a non-deformed cylindrical bubble with the same cross-section (volume) as that of the deformed bubble. With the increase of Φ, the radius of the wetting film, R_F, increases at the expense of the decrease of the radius of the meniscus region, R_P. For hexagonally packed, infinitely-long 2D-bubbles, R_F and R_P can be calculated by equations derived by Princen [3,4,32,33]:

$$R_F(\Phi) = R_0\left(\frac{\Phi_0}{\Phi}\right)^{1/2}\left[1-\left(\frac{1-\Phi}{1-\Phi_0}\right)^{1/2}\right] \tag{1}$$

$$R_P(\Phi) = R_0\left(\frac{\Phi_0}{1-\Phi_0}\right)^{1/2}\left(\frac{1-\Phi}{\Phi}\right)^{1/2} \tag{2}$$

where the air volume fraction $\Phi_0 = 0.9069$ corresponds to hexagonally close-packed circular cylinders of radius R_0. The length of the projection of the bubble on the surface of the solid wall, L, can be found from the geometrical relation

$$L(\Phi) = 2(R_F + R_P) = 2R_0\left(\frac{\Phi_0}{\Phi}\right)^{1/2} \tag{3}$$

The capillary pressure of the bubble is defined as $P_C = (P_B - P_0) = \sigma/R_P$, where P_B is the pressure inside the bubble, P_0 is the pressure of the aqueous phase in Plateau border region (PB region) away from the film, and σ is the surface tension.

In the consideration below we assume that R_F, R_P, L and P_C do not depend on the velocity of the moving solid wall, V_0, and can be determined by Eqs. (1)-(3), despite the fact that the thickness and the shape of the wetting film depend strongly on V_0. In other words, we assume that the moving wall leads to an increase of the liquid layer thickness in the bubble-wall contact zone, without affecting the curvature of the bubble surface far away from the wetting film.

The modification of the results obtained for 2D-bubbles to describe the friction in the film formed between an actual foam bubble (called for brevity 3D-film) and a solid wall is presented in Section 4.2. It is instructive to note from the very beginning that the relevant comparison of the 2D and 3D films with respect to foam-wall friction is at similar values of R_F and R_F/R_P. As seen from the comparison shown in Table 1, similar ratio R_F/R_P is observed at rather different air volume fractions in the case of 2D and 3D films. For example, the results for 2D systems with $\Phi = 0.925$, 0.965, and 0.985 should be compared with 3D systems having air volume fractions of $\Phi_{3D} \approx 0.733$, 0.872, and 0.945, respectively, because the respective ratios, R_F/R_P, are similar for the corresponding volume fractions.

2.2. Shape of the bubble surface in the contact zone.

In our previous study [11] we used the simplifying assumption that the fluid film surface had a certain pre-described shape. Two different profiles, linear and curved ones were compared, and we showed that the calculated friction forces differed by less than 3 % for these two film shapes. This result demonstrated that the assumption for a particular shape of the upper film surface does not affect strongly the final result for the calculated friction force.

In the current study we also use two model profiles for the fluid surface of the liquid layer, which are chosen as to allow us to account for the friction in both the film and the meniscus regions. In both model profiles, the meniscus region is represented by circular arcs of radius R_P (see Eqs. (4a)-(4c); (5a)-(5d) below), whereas for the film region we use two different shapes, linear and curved – see Figs. 2 and 3, and Eqs. (4b) and (5b)-(5c) below. The linear profile for the film region is chosen, because this is the simplest possible configuration of the system and it allows us to make a comparison with the results from our previous study [11]. The model curved profile in the current study was chosen to represent the main regions in the dynamic films, as observed in the experiments described in Section 5 below, cf. Figs. 3B and 3C (see also Refs. [34,35]).

(A) *Linear profile of the upper film surface.*

Here we assume that the bubble surface consists of three regions - two meniscus regions and one film region, which are connected as shown in Fig. 2. The first meniscus region, placed at the entrance of the film, is described by a circular arc with radius R_P and a geometrical center with co-ordinates $\{x_1 = R_P; z_1 = h_1 + R_P\}$, where x_1 is the position of the transition point between the meniscus and the film, and $h_1 = h(x=x_1)$ is the respective film thickness. Thus, the equation describing the entrance meniscus region is:

$$h(x) = h_1 + R_P - \sqrt{R_P^2 - (x - R_P)^2}\,; \qquad 0 \le x \le x_1 \tag{4a}$$

The profile of the bubble surface in the film region is assumed linear:

$$h(x) = h_1 + \frac{h_2 - h_1}{2R_F}(x - x_1); \qquad x_1 \le x \le x_2 \tag{4b}$$

where $x_2 = R_P + 2R_F$ corresponds to the end of the film region (the exit), and h_2 is the respective film thickness.

The profile of the bubble surface in the second PB region is described by a circular arc with radius R_P

$$h(x) = h_2 + R_P - \sqrt{R_P^2 - (x - x_2)^2}\,; \qquad x_2 \le x \le L \tag{4c}$$

where L is the x-coordinate of the end of the bubble projection on the wall surface, $L = 2R_F + 2R_P$.

The functions describing the linear profile contain two unknown geometrical constants: h_1 and h_2, which are found while solving the complete set of equations, as described in Section 2.4.

(B) *Curved profile of the upper film surface.*

The second model profile was constructed on the basis of microscope observations of the actual dynamic films between bubbles and moving solid wall (see Section 5.1 below for explanations about the experimental procedure). In Fig. 3A we show a typical photograph in reflected light of the contact region between a bubble and a moving solid wall. As explained in Section 5.1, from such a photograph one can reconstruct the profile of the upper surface of the wetting film, which is formed between the bubble and the moving wall, see Fig. 3B. One sees that the bubble surface has a complex shape, which consists of several distinct regions. To perform self-contained numerical calculations (without the necessity to use specific experimental information about the film shape and thickness), we approximated the bubble surface with a combination of several model functions: one parabolic and one cosine functions in the region of the wetting film, plus two circular arcs for the two meniscus regions around the film, see Fig. 3C. The parameters describing these functions are determined while solving the hydrodynamic problem for the liquid flow between the bubble and the wall, as described in Sections 2.3 and 2.4.

In this model, the bubble surface is divided into four regions, as shown in Fig. 3C: two meniscus regions (between 0 and x_0, and between x_2 and L), and two regions for the wetting film (between x_0 and x_1, and between x_1 and x_2). The following equations were used to describe these regions:

$$h(x) = h_{0c} + R_P - \sqrt{R_P^2 - (x - R_P)^2}\,; \qquad 0 \le x \le x_0 \tag{5a}$$

$$h(x) = h_1 + \frac{m(x - x_1)^2}{2R_P}; \qquad x_0 \le x \le x_1 \tag{5b}$$

$$h(x) = h_1 + \frac{h_2 - h_1}{2}\left[1 - \cos\left(\frac{\pi(x - x_1)}{x_2 - x_1}\right)\right]; \qquad x_1 \le x \le x_2 \tag{5c}$$

$$h(x) = h_2 + R_P - \sqrt{R_P^2 - (x - x_2)^2} \; ; \qquad x_2 \le x \le L \tag{5d}$$

Two important differences between the linear and curved model profiles are worthy mentioning:

(1) For the curved profile we assume that the transition between the circular arc and the parabola describing the first film region occurs at a coordinate x_0, which differs from R_P, whereas the transition between the meniscus and the film is assumed to occur always at $x_1 = R_P$ for the linear profile. For the curved profile, the transition point, x_0, is found by requiring equal slopes of the circular arc with radius R_P representing the meniscus region and the parabola representing the dynamic wetting film, see Eq. (6) below.

(2) To close the set of equations and based on the experimental observations (Section 5.2), we assume for the curved profile that the maximum of the dynamic pressure is always at the transition point between the parabola and the cosine function, while no such assumption is used for the linear profile.

The curved profile is described by three unknown constants – the thickness of the film at the transition between the parabola and the cosine function, h_1, the minimal thickness of the film, h_2, and the radius of curvature of the parabola describing the first film region, mR_P. The parameter m is the ratio of the curvatures of the parabola and the circular arc describing the meniscus region, R_P. All other geometrical parameters describing the shape of the upper film surface can be found from h_1, h_2 and m, by using the following relations:

The film thickness, $h_0=h(x=x_0)$ is determined from Eq. (5b). On its turn, x_0 is determined by matching the derivatives of the two functions $h(x)$ at the transition point, $x=x_0$, which leads to the following transcendental equation for x_0:

$$\frac{x_0 - R_P}{\sqrt{R_P^2 - (x_0 - R_P)^2}} = \frac{m(x_0 - x_1)}{R_P} \tag{6}$$

To determine the value of x_1, we pre-set the ratio of the film, which is occupied by the parabola and by the cosine function. For simplicity, we assume that the cosine function occupies always a given fraction of the film region, $(x_2\text{-}x_1) = k(2R_F)$, where k is assumed to be constant, which does not depend on the capillary number and on the air volume fraction. This assumption is in a reasonably good agreement with the experimental observations - see Fig. 12A below, in which the film shape is represented for different velocities, V_0. In addition, direct numerical calculations showed that the results for the friction force depend slightly on the chosen value of k, while the latter is varied between 0.1 and 0.3 (the range observed in the experiments). Thus, we set for the calculations: $x_1 = [R_P + 2(1\text{-}k)R_F]$ and $x_2 = (R_P + 2R_F)$. All numerical results presented below are obtained with $k = 0.1$.

Concluding, the curved film profile is characterized by three unknown constants, h_1, h_2 and m, which are determined while solving the overall problem, as explained at the end of Section 2.4.

2.3. Basic equations and boundary conditions.

For description of the liquid flow between the bubble and the solid wall we use the lubrication equation

$$\frac{dP}{dx} = \mu \frac{\partial^2 V_x}{\partial z^2} \tag{7}$$

where μ is the liquid viscosity and $P(x)$ is the local pressure in the liquid layer. In the lubrication approximation this pressure is a function of the x-coordinate only and does not depend on z. In contrast, the lateral component of the fluid velocity, $V_x(x,z)$, is a function of both coordinates, x and z. Due to the assumed 2D-configuration of the bubble, no dependence on y-coordinate is considered for any of the studied quantities. All intensive quantities, such as the friction force, F_{FR}, are given per unit length of the bubble.

Equation (7) is solved under the assumption that the bubble surface is tangentially immobile, which corresponds to the following boundary conditions for the fluid velocity at the upper and lower surfaces of the film

$$\begin{aligned} V_x(x, z = 0) &= V_0 \\ V_x(x, z = h) &= 0 \end{aligned} \tag{8}$$

where $h(x)$ is the local thickness of the liquid layer.

For determination of the dynamic pressure inside the liquid layer we use the following boundary conditions:

$$P(x = 0) = P(x = L) = P_0 \tag{9}$$

which implies that the pressure in the liquid between two neighbouring bubbles in the foam is equal. Note that this boundary condition is justified when studying the foam-wall friction with 3D foams, because the PB regions between the bubbles are interconnected. For some of the related research problems (e.g., bubble/drop moving in a capillary) the boundary condition, Eq. (9), should be modified, because the pressures on both ends of the bubble could be different.

The lubrication equation is solved along with the equation for mass conservation, which could be written in the following form [11,36]

$$Q = \int_0^h V_x(x,z)dz = \text{const} \tag{10}$$

Equation (10) expresses the fact that the hydrodynamic flux, Q, should be conserved along the film. The flux Q is not known in advance and has to be found while solving the entire hydrodynamic problem.

2.4. Set of equations solved numerically.

In this section we present the set of equations, which are solved to determine the geometrical parameters describing the film shape, as well as the equations used to determine the dynamic pressure inside the film, the viscous stress on the solid wall, and the friction force (see also the Appendix).

Double integration of Eq. (7) along with the boundary conditions, Eq. (8), leads to the following expression for the liquid velocity $V_x(x,z)$

$$V_x(x,z) = \frac{1}{2\mu}\frac{dP}{dx}z(z-h) - V_0\left(\frac{z}{h}-1\right) \tag{11}$$

By introducing Eq. (11) into Eq. (10), one derives the following equation for $P(x)$:

$$\frac{dP}{dx} = 6\mu\left[-\frac{2Q}{h^3} + \frac{V_0}{h^2}\right] \tag{12}$$

which is integrated to derive an expression for the dynamic pressure $P_d[h(x)]$

$$P_d(x) \equiv P(x) - P_0 = 6\mu\int_0^x\left[-\frac{2Q}{h^3} + \frac{V_0}{h^2}\right]dx \tag{13}$$

In the above equations, Q is unknown constant. By using the boundary condition $P_d(x = L) = 0$, one obtains the following expression for Q:

$$Q = \frac{V_0}{2}\left[\left(\int_0^L \frac{dx}{h^2}\right)\Big/\left(\int_0^L \frac{dx}{h^3}\right)\right] \tag{14}$$

The above equation is used for determination of Q for the linear profile of the upper film surface, Eqs. (4a)-(4c). For the curved film profile, Eqs. (5a)-(5d), we assumed that the maximum in the dynamic pressure occurs at $x = x_1$, i.e. $dP/dx = 0$ at $x = x_1$ (see Fig. 12A and Section 5.2 for argumentation), which leads to the relation $Q = V_0h_1/2$. The latter

approximation allowed us to use the boundary condition $P_d(x = L) = 0$ for determination of the unknown value of h_1 in the curved film profile.

For both profiles, linear and curved, the minimal film thickness, h_2, is determined from the normal force balance, which could be written in the following form (at negligible contribution of the disjoining pressure [11]):

$$\int_0^L P_d\left(x\right)dx = 2R_F P_C \tag{15}$$

Equation (15) implies that the dynamic pressure inside the film, $P_d(x) = P(x) - P_0$, which acts on the fluid film surface from below (defined as an excess with respect to the pressure in the liquid outside the film, P_0), is counterbalanced by the capillary pressure of the bubble, P_C.

The friction force on the solid surface is calculated by the equation:

$$F_{FR} = \left| \int_{A_B} \mu \left(\frac{\partial V_x}{\partial z} \right)_{z=0} dA \right| = 2\mu \int_0^L \left[-\frac{3Q}{h^2} + \frac{2V_0}{h} \right] dx \tag{16}$$

where A_B is the projected area of unit length of the bubble on the wall surface. The friction force is defined in Eq. (16) to be positive (despite the fact that it is directed opposite to the x-axis in the used coordinate system, Figure 1B).

Direct check with the final formulas confirmed that the friction force exerted on the wall, Eq. (16), is equal in magnitude and opposite in direction to the friction force acting on the bubble. Following the reasoning in Section 2.3 of Ref. [11], minimization of F_{FR} is used to determine the last unknown geometrical parameter, h_1, for the linear profile, Eqs. (4a)-(4c), and the parameter m characterizing the parabola for the curved film profile, Eqs. (5a)-(5d). Thus a closed set of equations is obtained (see also [37]).

It is more convenient to use dimensionless functions in the calculations, as well as for presenting and analyzing the results. For illustration, we present below the dimensionless equations for the linear profile of the film surface; the same scaling is used for the curved profile.

First, we introduce the dimensionless variables $\xi \equiv x/L$ and $\eta \equiv h(x)/h_C$, where the scaling constant for the film thickness is defined as:

$$h_C \equiv \left(\frac{\mu V_0 R_F}{P_C} \right)^{1/2} = Ca^{1/2} \left(R_F R_P \right)^{1/2} \tag{17}$$

The dimensionless liquid flux along the film is defined as $\widetilde{Q} \equiv Q/(V_0 h_C)$ and Eq. (14) can be expressed in the form:

$$\tilde{Q}=\frac{1}{2}\left\{\frac{\int_0^1 \frac{d\xi}{\left[\eta(\xi)\right]^2}}{\int_0^1 \frac{d\xi}{\left[\eta(\xi)\right]^3}}\right\}=\frac{1}{2}\left\{\frac{\int_0^{\xi_1} \frac{d\xi}{\left[\eta_{\mathrm{I}}(\xi)\right]^2}+\int_{\xi_1}^{\xi_2} \frac{d\xi}{\left[\eta_{\mathrm{II}}(\xi)\right]^2}+\int_{\xi_2}^1 \frac{d\xi}{\left[\eta_{\mathrm{III}}(\xi)\right]^2}}{\int_0^{\xi_1} \frac{d\xi}{\left[\eta_{\mathrm{I}}(\xi)\right]^3}+\int_{\xi_1}^{\xi_2} \frac{d\xi}{\left[\eta_{\mathrm{II}}(\xi)\right]^3}+\int_{\xi_2}^1 \frac{d\xi}{\left[\eta_{\mathrm{III}}(\xi)\right]^3}}\right\} \tag{18}$$

where $\eta_{\mathrm{I}}(\xi)$, $\eta_{\mathrm{II}}(\xi)$ and $\eta_{\mathrm{III}}(\xi)$ is the dimensionless thickness in the first meniscus region, in the film region, and in the second meniscus region, respectively (see Fig. 2 and Eqs. (4a)-(4c)), whereas $\xi_1 = x_1/L$ and $\xi_2 = x_2/L$ are the dimensionless positions of the film entrance and film exit, respectively. The integration of the functions in Eq. (18), gives an analytical expression for the dependence of $\tilde{Q}$ on the parameters η_1 and η_2, which are still unknown constants:

$$\tilde{Q}=\frac{\left(\frac{1}{\eta_1\eta_2}+\frac{1}{2}G^{1/2}\left(\frac{1}{\eta_1(2+\delta_1)}+\frac{1}{\eta_2(2+\delta_2)}\right)+\frac{1}{2}G^{1/4}\left(\frac{R_P}{R_F}\right)^{1/2}\left(\frac{\frac{\pi}{2}+\arcsin\frac{1}{1+\delta_1}}{\eta_1^{3/2}(2+\delta_1)^{3/2}}+\frac{\frac{\pi}{2}+\arcsin\frac{1}{1+\delta_2}}{\eta_2^{3/2}(2+\delta_2)^{3/2}}\right)\right)}{\left(\frac{\eta_1+\eta_2}{\eta_1^2\eta_2^2}+\frac{1}{2}G^{1/2}\left(\frac{2(1+\delta_1)^2+1}{\eta_1^2(2+\delta_1)^2(1+\delta_1)}+\frac{2(1+\delta_2)^2+1}{\eta_2^2(2+\delta_2)^2(1+\delta_2)}\right)+\frac{3}{2}G^{1/4}\left(\frac{R_P}{R_F}\right)^{1/2}\left(\frac{\left(\frac{\pi}{2}+\arcsin\frac{1}{1+\delta_1}\right)(1+\delta_1)}{\eta_1^{5/2}(2+\delta_1)^{5/2}}+\frac{\left(\frac{\pi}{2}+\arcsin\frac{1}{1+\delta_2}\right)(1+\delta_2)}{\eta_2^{5/2}(2+\delta_2)^{5/2}}\right)\right)} \tag{19}$$

where the dimensionless quantities $G = (R_P/R_F)Ca$ and $\delta_{1,2} = (h_{1,2}/R_P) = \eta_{1,2}(CaR_F/R_P)^{1/2}$ are introduced.

By using Eqs. (13) and (17) one derives the following equation for the dimensionless dynamic pressure in the layer between the bubble and the wall:

$$\tilde{P}_d(\xi) \equiv P_d(\xi)/P_C = 6\frac{L}{R_F}\int_0^{\xi}\left(\frac{\eta(\xi)-2\tilde{Q}}{\left[\eta(\xi)\right]^3}\right)d\xi \tag{20}$$

where $\tilde{Q}$ is determined from Eq (19). Introducing Eq. (19) into Eq. (15), one derives the following transcendental equation (representing the normal force balance) for determination of the minimal film thickness, h_2, and its dimensionless counterpart, η_2:

$$\frac{R_F^2}{L^2} = 3\int_0^1 d\xi\int_0^{\xi}\left(\frac{\eta(\xi)-2\tilde{Q}}{\left[\eta(\xi)\right]^3}\right)d\xi \tag{21}$$

To determine the remaining parameter h_1 and the friction force, we proceed as follows: From Eq. (16) we express the friction force in the form

$$\tilde{F}_{FR} = 2\int_0^1 \left(\frac{2\eta(\xi) - 3\tilde{Q}}{\left[\eta(\xi)\right]^2} \right) d\xi =$$
$$\left[\tilde{F}_{FR}^{(1)} + \tilde{F}_{FR}^{(2)} + \tilde{F}_{FR}^{(3)} \right] =$$
$$= 2\left[\int_0^{\xi_1} \left(\frac{2\eta_I(\xi) - 3\tilde{Q}}{\left[\eta_I(\xi)\right]^2} \right) d\xi + \int_{\xi_1}^{\xi_2} \left(\frac{2\eta_{II}(\xi) - 3\tilde{Q}}{\left[\eta_{II}(\xi)\right]^2} \right) d\xi + \int_{\xi_2}^{1} \left(\frac{2\eta_{III}(\xi) - 3\tilde{Q}}{\left[\eta_{III}(\xi)\right]^2} \right) d\xi \right] \tag{22}$$

where the dimensionless friction force was introduced

$$\tilde{F}_{FR} = F_{FR} / \left[\sigma Ca^{1/2} \frac{L}{\left(R_F R_P\right)^{1/2}} \right] = F_{FR} / \left[2\sigma Ca^{1/2} \frac{\left(R_F + R_P\right)}{\left(R_F R_P\right)^{1/2}} \right] = F_{FR} \left[R_{FP} / 2\sigma h_C \right] \tag{23}$$

$R_{FP} = (1/R_F + 1/R_P)^{-1}$ is the harmonic mean of R_F and R_P. Respectively, $\tilde{F}_{FR}^{(1)}$ in Eq. (22) is the dimensionless friction force in the first meniscus region (before the film entrance), $\tilde{F}_{FR}^{(2)}$ - in the film region, and $\tilde{F}_{FR}^{(3)}$ - in the second meniscus region (after the film exit). Analytical integration of the friction stress over the different regions results in the following expressions for the three components of the friction force:

$$\tilde{F}_{FR}^{(1)} = \frac{2h_C}{L} \left(\frac{\frac{\pi}{2} + \mathrm{ArcSin}\left(\frac{1}{1+\delta_1} \right)}{\eta_1 \sqrt{\left(1 + 2/\delta_1\right)}} \left(2\eta_1 + 2\frac{\eta_1}{\delta_1} - \frac{3\tilde{Q}}{\delta_1\left(2+\delta_1\right)} \right) - \pi - \frac{3\tilde{Q}}{\eta_1\left(2+\delta_1\right)} \right) \tag{24a}$$

$$\tilde{F}_{FR}^{(2)} = \frac{4R_F}{L} \left(\frac{2}{\eta_1 - \eta_2} \ln\frac{\eta_1}{\eta_2} - \frac{3\tilde{Q}}{\eta_1\eta_2} \right) \tag{24b}$$

$$\tilde{F}_{FR}^{(3)} = \frac{2h_C}{L} \left(\frac{\frac{\pi}{2} + \mathrm{ArcSin}\left(\frac{1}{1+\delta_2} \right)}{\eta_2 \sqrt{\left(1 + 2/\delta_2\right)}} \left(2\eta_2 + 2\frac{\eta_2}{\delta_2} - \frac{3\tilde{Q}}{\delta_2\left(2+\delta_2\right)} \right) - \pi - \frac{3\tilde{Q}}{\eta_2\left(2+\delta_2\right)} \right) \tag{24c}$$

The last step in solving the set of equations is to minimize the total friction force [11], F_{FR}, in order to determine the value of η_1.

Thus the numerical procedure for the linear film profile can be summarized as follows: (1) the dimensionless flux, $\widetilde{Q}$ is expressed from Eq. (19) as a function of the unknown parameters η_1 and η_2; (2) The parameter η_2 is determined as a function of η_1 from Eq. (21); (3) From minimization of the friction force we determine the value of η_1, which is substituted into Eqs. (18)-(24) to evaluate η_2, $\widetilde{Q}$, $P_d(\xi)$, and $\tilde{F}_{FR}$ for given values of *Ca* and Φ. The relative contributions of the meniscus and film regions in the total friction force are determined from the ratios $f_P = \left(\tilde{F}_{FR}^{(1)} + \tilde{F}_{FR}^{(3)}\right)\Big/\tilde{F}_{FR}$ and $f_{FILM} = \tilde{F}_{FR}^{(2)}/\tilde{F}_{FR}$.

The corresponding expressions for the curved film profile are presented in the Appendix. The numerical procedure in this case is the following: (1) The dimensionless flux, $\widetilde{Q}$, is assumed equal to $\eta_1/2$; (2) The dimensionless thickness, η_1, is expressed as a function of *m* and η_2 from the counterpart of Eq. (18); (3) Equation (21) is used for determination of η_2 at a given value of *m*; (4) From minimization of the total friction force, the value of *m* is determined and, afterwards, substituted into Eqs. (18)-(22) to determine η_1, η_2, $P_d(\xi)$,and $\tilde{F}_{FR}$ for given values of *Ca* and Φ.

3. Numerical results.

First, we present and compare numerical results for the friction force, as calculated with the two model profiles of the film surface, the linear and the curved ones. These results show that: (1) the friction forces calculated with the two profiles are very similar at equivalent *Ca* and Φ, and (2) two qualitatively different cases could be distinguished, depending on the value of Φ (viz. on the ratio R_F/R_P) – at high air volume fraction the viscous friction inside the wetting film dominates, whereas at lower air volume fraction the contributions of the viscous stress inside the film and in the transition region film-meniscus are comparable. Appropriate scaling laws are suggested to describe the dependence of the friction force on *Ca* and on the ratio R_F/R_P. Afterwards, we show typical numerical results for the shape of the bubble surface, dynamic pressure and distribution of the viscous stress along the solid wall, as calculated with the curved profile of the upper film surface. The calculations are limited to small capillary numbers, $Ca \leq 10^{-2}$, to remain in the range, in which the lubrication approximation is expected to be valid [18].

3.1. Friction force.

The dependence of the dimensionless friction force, $\tilde{F}_{FR}$, on the capillary number, *Ca*, is shown in Fig. 4A,B at several air volume fractions, varying between Φ = 0.93 and 0.999.

Fig. 4A shows the results calculated with the linear film profile and Fig. 4B – with the curved film profile, whereas Fig. 4C is a correlation plot for the results calculated with these two model profiles. From Fig. 4C one sees that the agreement between the numerical results calculated with the two model profiles is very good (typically within a few percent), except for the lowest air volume fraction, $\Phi = 0.93$ (see the empty squares in Fig. 4C). From this correlation plot one can conclude that the assumed specific shape of the bubble surface does not affect strongly the calculated force, except for the lowest air volume fractions, corresponding to $\Phi_{3D} \approx 0.75$, and hence, in the following consideration we discuss the general trends for both profiles together.

One sees from Fig. 4A,B that $\tilde{F}_{FR}$ is almost constant at $\Phi = 0.999$ ($R_F/R_P \approx 9$), which means that the dimensional friction force scales very well with $Ca^{1/2}$, see Eq. (23). At such high air volume fractions, the friction in the film dominates – the numerical results practically coincide with those calculated in Ref. [11], where we neglected the friction in the meniscus region. However, at lower air volume fractions, $\Phi \le 0.99$ ($R_F/R_P \le 2$), the dimensionless force $\tilde{F}_{FR}$ is lower and increases with the capillary number Ca. These trends reflect the fact that the total friction force includes a noticeable contribution from the transition regions film-meniscus under these conditions. The relative contributions of the friction inside the film, f_{FILM}, and in the transition regions film-meniscus, f_P, are compared in Fig. 5 - one sees that the ratio f_P/f_{FILM} depends strongly on both Ca and Φ. At high air volume fractions, $\Phi \ge 0.99$ ($R_F/R_P \ge 2$), the friction inside the film region is prevailing. In contrast, at lower air volume fractions, f_P could be larger than f_{FILM}. At fixed Φ, the relative contribution of the friction in the transition zones film-meniscus increases strongly with the capillary number.

The relative contributions of the friction in the various regions is further analysed in the Appendix. After an expansion of Eqs. (24a)-(24c) in series, taking the leading terms with respect to Ca, and interpolating the numerical results by the least-squares method, we found that the total friction force could be described rather well by the following expression:

$$F_{FR} \approx 2.50\sigma Ca^{1/2}\left(\frac{R_F}{R_P}\right)^{1/2} + \sigma\left(7.0Ca^{3/4} - 8.5\left(\frac{R_P}{R_F}\right)^{1/4} Ca\right) \qquad \text{(curved profile)} \qquad (25)$$

The first term in Eq. (25) accounts for the friction inside the film and is equivalent to the force calculated in our previous study [11]. The remaining two terms account for the friction in the transition regions film-meniscus; the numerical constants in front of $Ca^{3/4}$ and Ca (7.0 and 8.5, respectively) were found in the interpolation procedure.

In Fig. 6A we show a comparison of the numerically calculated values of $\tilde{F}_{FR}$ (the symbols) and those calculated from Eq. (25) (the solid curves) - a relatively good agreement, typically within a few percent, is established for all values of Ca and Φ of interest ($Ca \le 10^{-2}$ and $\Phi \ge 0.93$, see Table 1 for the corresponding volume fraction of 3D-bubbles, Φ_{3D}).

Noticeable deviations are observed only when the air volume fraction is very low, $\Phi \approx 0.93$ (corresponding to $\Phi_{3D} \approx 0.75$) and the capillary numbers are relatively high, $Ca > 10^{-4}$, but even these deviations do not exceed 15 %.

Remarkably, we found by direct numerical comparison that the last two terms in Eq. (25), which account for the friction in the transition regions film-meniscus, could be approximated rather well in a certain range of capillary numbers and air volume fractions by an expression, which scales with $Ca^{2/3}$, as suggested by Bretherton [18] (who neglected the friction inside the film). In this range, Eq. (25) can be presented as

$$F_{FR} \approx 2.50\sigma Ca^{1/2}\left(\frac{R_F}{R_P}\right)^{1/2} + 3.3\sigma Ca^{2/3} \qquad (P_C = \sigma/R_P) \quad (25')$$

The latter equation described relatively well (accuracy better than 5 %) the calculated values for the friction force at $10^{-7} \le Ca < 10^{-3}$. However, a systematic deviation was observed at higher capillary numbers, $Ca > 10^{-3}$, with Eq. (25') predicting larger friction force than the numerical calculations – see the dashed curves in Fig. 6A. Equation 25' is very convenient for estimating and comparing the contributions of the friction stresses in the film region and in the transition region film-meniscus.

It is worthwhile noting that the numerical factor 3.3 in front of the second term in Eq. (25'), is about twice smaller than the numerical factor 7.46 given in the Bretherton's paper for bubbles with tangentially immobile surface in the transition region film-meniscus (Bretherton always assumes that the flow inside the film is a plug-flow, which corresponds to mobile surface at the entrance of the planar film) [18, 38]. Note also that different definitions of the capillary pressure are used in the two models: since we consider infinitely long 2D-bubbles, we define $P_C = \sigma/R_P$, whereas Bretherton considered a bubble moving in a capillary tube, so that $P_C = 2\sigma/R_P$ in his model [18]. This difference in the definitions of P_C affects the normal force balance, Eq. (15). We checked numerically how the change of the capillary pressure definition into $P_C = 2\sigma/R_P$ affects the predictions of our model, and found that the numerical pre-factor for the friction in the film region increases by $2^{1/2}$ (such change is predicted also by our previous model [11]), whereas the numerical factor for the friction in the transition zone increases by less than 10 %:

$$F_{FR} \approx 2.50\sqrt{2}Ca^{1/2}\sigma\left(\frac{R_F}{R_P}\right)^{1/2} + 3.6Ca^{2/3}\sigma \qquad (P_C = 2\sigma/R_P) \quad (25'')$$

Thus the numerical factor for the friction in the transition zones film-meniscus still remains smaller than the respective factor in the Bretehrton's model [18,38], due to the coupling between the friction in the film and in the transition regions for bubbles with tangentially immobile surfaces (see also the discussion in Section 6).

3.2. Shape of the bubble surface.

The shape of the bubble surface for the curved profile is determined by Eqs. (5a)-(5d). To compare the bubble shapes at different capillary numbers, we present in Fig. 7 the dimensionless film thickness, $\eta = h/h_C$, as a function of the scaled coordinate, $\xi = x/L$, as calculated at $Ca = 10^{-3}$ and $Ca = 10^{-5}$ for given, relatively high air volume fraction, $\Phi = 0.99$ (corresponding to $\Phi_{3D} \approx 0.96$). One sees from Fig. 7 that the thickness of the liquid layer inside the film region scales very well with $Ca^{1/2}$. However, the thickness of the liquid layer in the PB regions does not scale with $Ca^{1/2}$, see Fig. 7. The latter result could be explained by analysing the equations describing the shape of the PB regions, Eqs. (5a) and (5d), which can be presented in the following dimensionless form:

$$\eta(\xi) = \eta_{0C} + \frac{L}{h_C}\left[\frac{R_P}{L} - \sqrt{\left(\frac{R_P}{L}\right)^2 - \left(\xi - \frac{R_P}{L}\right)^2}\right]; \quad 0 \le \xi \le \xi_0 \qquad (5a')$$

$$\eta(\xi) = \eta_2 + \frac{L}{h_C}\left[\frac{R_P}{L} - \sqrt{\left(\frac{R_P}{L}\right)^2 - (\xi - \xi_2)^2}\right]; \qquad \xi_2 \le \xi \le 1 \qquad (5d')$$

The numerical calculations show that the values of η_{0C} and η_2 vary within less than 1 %, while varying the capillary number at such high value of the air volume fraction, $\Phi = 0.99$, whereas the second terms in the right-hand-sides of Eqs. (5a') and (5d') are multiplied by $L/h_C \sim Ca^{-1/2}$. Thus the dimensionless thickness in the PB region should decrease with the increase of Ca, just as observed in the numerical calculations.

The effect of air volume fraction, Φ, on the bubble shape at fixed capillary number, $Ca = 10^{-3}$, is illustrated in Fig. 7B. The higher air volume fraction leads to larger film radius, see Eq. (1), and to smaller dimensionless film thickness in both the film and the PB regions. For example, the value of $\eta_2 = h_2/h_C$ decreases by ≈ 40 % (from 0.82 down to 0.5) when Φ increases from 0.95 to 0.99. On the other hand, the value of h_C increases only by 3 % (from 0.43 to 0.45) while increasing Φ from 0.95 to 0.99. Thus, the dimensional film thickness is around 40 % smaller at higher value of Φ, for the same bubble radius. This reduction of the film thickness is due to the higher capillary pressure of the more deformed bubbles at higher air volume fraction.

The dependence of the main geometrical parameters characterizing the film thickness, η_1 and η_2, on Φ and Ca is illustrated in Fig. 8. The values of η_1 and η_2 decrease with the increase of Φ (due to the increased capillary pressure of the deformed bubbles) and reach a constant value of 0.83 and 0.45, respectively, when $\Phi \ge 0.99$ and the friction in the film dominates the total friction force. The dependence of the dimensionless film thickness on Ca

is rather weak at such high air volume fractions. In contrast, at lower volume fractions, when the friction in the transition region film-meniscus is significant, the dimensionless film thickness increases rapidly with the increase of *Ca*.

By fitting the numerical data for the film thickness, h_1 and h_2, we constructed the following semi-empirical expressions to describe their dependence on *Ca*, R_F, and R_P:

$$\frac{h_1}{R_P} \approx 0.83 Ca^{1/2} \left(\frac{R_F}{R_P} \right)^{1/2} + 0.42 \frac{R_P}{R_F} Ca^{0.7} \tag{26}$$

$$\frac{h_2}{R_P} \approx 0.45 Ca^{1/2} \left(\frac{R_F}{R_P} \right)^{1/2} + 0.29 \frac{R_P}{R_F} Ca^{0.7} \tag{27}$$

Equations (26) and (27) describe all numerical results with accuracy better than 5 %. These equations show that the effects of Φ (expressed through the values of R_F and R_P) and *Ca* could be decomposed into two groups, one of them proportional to $(CaR_F/R_P)^{1/2}$, which accounts for the viscous stress inside the film, whereas the other one is proportional to (R_P/R_F) $Ca^{0.7}$. The first group dominates at high volume fractions, when the friction inside the film prevails in the total friction force. At lower volume fraction, the two terms are comparable. The attempt to describe the numerical results for the film thickness by using a linear combination of the predictions of the two models (Refs. [11] and [18]), viz. $h \propto (A_1 \mathrm{Ca}^{1/2} + A_2 Ca^{2/3})$, where A_1 and A_2 are numerical constants, gave noticeably worse description.

3.3. Stress distribution on the wall surface.

The viscous stress on the solid wall can be calculated from the velocity profile $V(x,z)$:

$$\tau = -\mu \left. \frac{\partial V_x}{\partial z} \right|_{z=0} = \frac{\mu V_0}{h_C} \left(\frac{4\eta(\xi) - 6\tilde{Q}}{\left[\eta(\xi)\right]^2} \right) \tag{28}$$

The sign of τ was chosen to be positive when the wall stress is directed in parallel with the friction force. The respective dimensionless viscous stress can be defined as

$$\tilde{\tau} = \tau / \left(\frac{\mu V_0}{h_C} \right) = \tau / \left[P_C \left(\frac{R_P}{R_F} Ca \right)^{1/2} \right] = \left(\frac{4\eta(\xi) - 6\tilde{Q}}{\left[\eta(\xi)\right]^2} \right) \tag{29}$$

As explained in Section 2.2, for the curved profile of the upper film surface we used the relation $\tilde{Q} = \eta_1 / 2$, which leads to:

$$\tilde{\tau} = \left(\frac{4\eta(\xi) - 3\eta_1}{\left[\eta(\xi)\right]^2} \right) \qquad (29')$$

From Eq. (29') one sees that the viscous stress is zero, when the dimensionless film thickness $\eta(\xi) = 0.75\eta_1$. The calculated surface profiles show that the latter condition is satisfied in the film region, which is approximated by a cosine function (see Eq. (5c)) and in the second meniscus region (Eq. (5d)). For all values $\eta(\xi) > 0.75\eta_1$ the stress is positive, whereas at $\eta(\xi) < 0.75\eta_1$ the stress is negative. Analytical differentiation of Eq. (29'), shows also that the stress passes through a maximum at $\eta(\xi) = 1.5\eta_1$, which occurs in the first film region (the parabola given by Eq. (5b)) and in the second meniscus region.

These features of the dependence $\tilde{\tau}(\xi)$ are illustrated in Fig. 9A with calculations performed at $\Phi = 0.99$ and two values of the capillary number, $Ca = 10^{-4}$ and 10^{-2}. For both capillary numbers the viscous stress passes through a relatively flat maximum inside the wetting film at $\xi \approx 0.4$ (slightly before the film centre). In the first film region, the ratio η/η_1 varies between 2.0 and 1.0, so that the stress is positive and relatively high. When the thickness of the film becomes smaller than $0.75\eta_1$ the stress becomes negative and passes through a deep and sharp minimum, which appears at the constriction point, ξ_2, where $d\eta/d\xi = 0$. A second maximum of the stress is observed in the PB region, after the film exit. This complex profile of the viscous stress reflects the changes of the velocity profile in the film and in the adjacent meniscus regions. For example, the negative stress (directed opposite to the total friction force), which observed at $\xi \approx 0.85$, is due to intensive Poiseuille flow in the narrow exit region (the constriction), created by the higher dynamic pressure in the film, $P > P_0$. In the constriction zone this Poiseuille flow prevails over the linear flow (directly created by the moving wall), which results in a local change of the sign of the fluid velocity gradient at the wall surface, $(\partial V_x/\partial z)_{z=0}$, see Eq. (28).

It is seen from Fig. 9A that the dimensionless stress, $\tilde{\tau}(\xi)$, is almost the same in the film region at the different capillary numbers, i.e., the stress scales with $Ca^{1/2}$ inside the film, see Eq. (29). However the stress in the PB regions is noticeably higher at the higher Ca number, because it does not scale with $Ca^{1/2}$. The numerical calculations show that at this air volume fraction, $\Phi_2 = 0.99$, the contribution of the viscous friction in the transition regions film-meniscus becomes noticeable at high capillary numbers, $Ca > 10^{-4}$, see Fig. 5. In contrast, the relative contribution of the viscous friction in the transition regions is important at all capillary numbers of interest when the air volume fraction is lower, see Eq. (25) and Fig. 5. As a result, the viscous stress does not scale with $Ca^{1/2}$ even in the film region at low values of Φ - see for example Fig. 9B, which plots the distribution of the viscous stress on the wall at $\Phi = 0.95$, and $Ca = 10^{-4}$ and 10^{-2}.

3.4. Dynamic pressure, P_d.

The dynamic pressure, P_d, gradually increases at the film entrance, passes through a maximum at $h = h_1$, and afterwards decreases rapidly in the narrow constriction region, passing through a shallow minimum and becomes zero at the end of the second PB region, see Fig. 10. The dependence of the dimensionless dynamic pressure on the scaled lateral coordinate is almost the same for different values of *Ca*, when the air volume fraction is relatively high and the friction in the film is dominant, see Fig. 10A. In contrast, the pressure distribution depends strongly on *Ca* at low air volume fractions - as seen from Fig. 10B, the dimensionless dynamic pressure in the PB regions increases, whereas it decreases inside the wetting film with the increase of *Ca*. This result is in agreement with the fact that the relative contribution of the viscous friction inside the meniscus regions increases with the capillary number, *Ca*, and is very significant at low values of Φ.

In conclusion of Section 3, the numerical results show that we could decompose the total friction into components related to the friction inside the wetting film and friction in the transition regions film-meniscus. At high air volume fractions, the friction in the film dominates and most of the quantities scale as described in our previous study [11]. At low air volume fractions, the friction in the transition regions film-meniscus is not negligible and more complex scaling laws are applicable, e.g., Eqs. (25), (25'), (26) and (27).

4. Viscous stress for foam-wall friction.

Following the approach from Section 2.5 in Ref. [11], here we use the expression for the friction force between a single bubble and a wall to calculate the average foam-wall viscous stress, τ_W, which is experimentally accessible quantity, e.g., by rheological measurements. For simplicity, in the derivation we use the shorter equation for the bubble-wall friction force, Eq. (25'). The same approach can be used to obtain analogous expression for τ_W, which is based on the more accurate Eq. (25).

4.1. Estimate of the average foam-wall viscous stress for 2D-films.

The average wall stress, τ_W, and the friction force per one bubble, F_{FR}, are related through the equation

$$\tau_W = F_{FR} / A_B \tag{30}$$

where A_B is the average area, occupied by one bubble on the solid wall. For two-dimensional bubbles like those considered in the preceding section, A_B is equal to $L = 2(R_P+R_F)$. Thus combining Eq. (25') and (30), we obtain the following expression for the average dimensionless friction stress on the wall:

$$\tilde{\tau}_W \equiv \left(\tau_W \frac{R_0}{\sigma}\right) = \frac{F_{FR}}{2\sigma} \frac{R_0}{\left(R_F + R_P\right)} \approx \left[1.25Ca^{1/2}\left(\frac{R_F}{R_P}\right)^{1/2} + 1.65Ca^{2/3}\right] \frac{R_0}{\left(R_F + R_P\right)} \approx$$

(2D-film)

$$1.25Ca^{1/2}\left(\frac{\Phi}{\Phi_0}\right)^{1/2}\left[\left(\frac{1-\Phi_0}{1-\Phi}\right)^{1/2} - 1\right]^{1/2} + 1.65Ca^{2/3}\left(\frac{\Phi}{\Phi_0}\right)^{1/2} \tag{31}$$

where R_0 is the radius of the non-deformed bubble, $\Phi_0 = 0.9069$ is the volume fraction at close-packing of the cylindrical 2D-bubbles, and R_F and R_P are expressed through Eqs. (1) and (2).

4.2. Estimate of the average foam-wall viscous stress for 3D-films.

As explained in Ref. [11], to estimate the foam-wall viscous stress for a real foam, which forms circular 3D-wetting films upon contact with the solid wall, we can assume that the average stress inside the 3D-film is proportional to the average viscous stress in the respective 2D-film (at equivalent all other conditions – bubble and film radii, surface tension, liquid viscosity, velocity of the substrate, etc.). For the friction in the transition zone film-meniscus, we assume that its contribution into the 3D-film is proportional to the respective friction contribution in the 2D-film, multiplied by the projected length of the 3D-film in direction perpendicular to the flow [6,11,39]. For the system under consideration, this projected length is equal to $2R_F$, where R_F is the radius of the 3D film.

Following this reasoning, we obtain the counterpart of Eq. (31) in the following form:

$$\tilde{\tau}_W = \left[C_{IFilm}\,1.25Ca^{1/2}\left(\frac{R_F}{R_P}\right)^{1/2} + C_{ILine}\frac{6.6}{\pi}Ca^{2/3}\right]\left(\frac{R_F}{R_0}\right) \quad \text{(3D-film)} \tag{32}$$

where the proportionality constants C_{IFilm} and C_{ILine} are introduced to account for the fact that we use the expression derived for the friction force of 2D-film to estimate the wall stress for 3D-films. The index "I" reminds that these expressions are for immobile bubble surface.

Further, to express the dependences of R_F and R_P on Φ_{3D}, one can use the function $f_3(\Phi_{3D}) = A_F/A_B$, which describes the relative area of the solid wall, which is covered by the wetting films and which was experimentally determined by Princen [5] to be given by the following empirical relation

$$f_3\left(\Phi_{3D}\right) \approx 1 - 3.2\left(\frac{\Phi_{3D}}{1-\Phi_{3D}} + 7.7\right)^{-1/2} \tag{33}$$

Assuming as reasonable approximations [11,40]

$$\left(R_F / R_0\right) \approx f_3^{1/2}\left(\Phi_{3D}\right) \tag{34}$$

$$A_B \approx \pi R_0^2 \approx \pi\left(R_F + R_P\right)^2 \tag{35}$$

one obtains

$$\tilde{\tau}_W = \left(\tau_W \frac{R_0}{\sigma}\right) = \left(C_{IFilm} 1.25 Ca^{1/2} \frac{f_3^{1/4}}{\sqrt{1-f_3^{1/2}}} + 2.1 C_{ILine} Ca^{2/3}\right) f_3^{1/2}$$

(3D-films, tangentially immobile bubble surface) (36)

The values of C_{IFilm} and C_{ILine} can be found by comparing the predictions of Eq. (36) with experimental results or with numerical calculations for 3D-films. The comparison with the experimental data for foam-wall friction, shown in Fig. 8C of Ref. [11], gave $C_{\mathrm{IFilm}} \approx 3.7$ (after neglecting the second term in Eq. (36), which is about an order of magnitude smaller than the first one). This value is about 20 % smaller than the value given in Ref. [11], $C_{\mathrm{IFilm}} \approx 4.6$, which is due to the different approximations used in the two papers, cf. Eq. (36) above with Eq. (2.42) in [11]. Further experimental and/or theoretical data are needed to determine the value of C_{IFilm} with better precision and to find the value of C_{ILine}.

5. Experimental check of the model predictions about the film thickness.

In this section we present experimental results from optical microscope observations of the dynamic wetting films, formed between bubbles and moving solid wall. These observations reveal the typical regions in the film, and allow determination of its thickness and shape. The regions observed experimentally in the dynamic films have been implemented in the theoretical consideration to design the curved model film profile, Eqs. (5a)-(5d). At the end of the current section, we compare the experimentally determined thickness of the dynamic films with the theoretical predictions.

5.1. Materials and methods.

Following our previous study [11], we performed the experiments with a solution of mixed potassium carboxylates having relatively long hydrocarbon tails (12 to 18 carbon atoms). The surfactant solution contained 0.5 wt % potassium laurate, 1 wt % potassium myristate, 0.5 wt % potassium palmitate, and 0.1 wt % potassium stearate (prepared by mixing KOH with the respective carboxylic acids, which were products of Uniqema, DE, and Research Organics, OH, USA). Glycerol (product of Teokom Co., Bulgaria) was used in some of the experiments to increase the viscosity of the aqueous phase. The water-glycerol-surfactant mixtures were first heated for 1 h at 50 °C to dissolve the surfactants, then cooled down to room temperature, and the pH was adjusted to 10.2 ± 0.1 with hydrochloric acid. The formed precipitate of soap particles was removed by centrifugation and filtration through 0.45 μm filter, just before the actual experiments with the foam bubbles. The solution prepared in this way exhibited very high surface modulus, E_S > 200 mN/m, when measured by the oscillating drop method at a frequency of 0.125 Hz. As a result, the bubble surface behaved as tangentially immobile [11]. The surface tension of the solutions, σ, was measured by the drop shape analysis on DSA10 instrument (Kruss GmbH, Germany), whereas the viscosity of the filtered solution, μ, was measured to be equal to that of pure water (within several percent).

The thickness of the dynamic wetting film, formed between a bubble and sliding solid wall, was measured in the equipment sketched in Fig. 11. Single bubble was formed on the tip of a stainless needle (external diameter 0.94 mm), which was placed inside a glass capillary tube (i.d. 1.17 mm) filled with surfactant solution. The diameter of the bubble was adjusted to be about 10 % smaller than the internal diameter of the glass capillary, so that a wetting film was formed between the bubble and the upper side of the capillary wall, under the action of the buoyancy force. Since the zone of contact in this experiment was formed between a spherical bubble and the cylindrical inner wall of the capillary, the wetting film had approximately elliptical shape with very large aspect ratio (> 7) between the long and short axes. Therefore, this configuration represented reasonably well the two-dimensional (2D) films between a bubble and wall, which were considered theoretically in the preceding sections – see for example the photograph in Fig. 3A.

The bubble and the wetting film were observed with optical microscope (Axioplan, Zeiss, Germany) in reflected monochromatic light with wavelength, λ = 546 nm, see Fig. 11. The dynamic films had complex shape of the air-water interface, which was determined by using the interference pattern observed in reflected light, see Fig. 3A. To analyse this interference pattern we used the known relation [41] between the intensity of the reflected light and the thickness of the film:

$$h = \frac{\lambda}{2\pi n_S}\left[(q+1)\pi/2 + \arcsin\sqrt{\frac{I - I_{MIN}}{I_{MAX} - I_{MIN}}}\right] \tag{37}$$

where n_s = 1.33 is the refractive index of the solution, q = 0, 1, 2, … is the order of interference, $I(x)$ is the local intensity of the light reflected from the liquid layer, I_{MAX} and I_{MIN} are the maximum and the minimum intensities of the reflected light, respectively (for a rigorous consideration see Ref. [41]). Equation (37) shows that the difference in the thickness between two consecutive interference stripes (dark to bright or bright to dark) is equal to $\lambda/4n_S \approx 102$ nm. The details in the procedure for interpretation of the microscope images, as well as a large set of results obtained with 2D- and 3D-films and various surfactants will be presented in a separate paper [35].

During the experiment, the glass capillary is translated with velocity, V_0, by a computer-controlled motor (Fauhaber, Germany), while the bubble remains stationary with respect to the laboratory frame. This experiment differs from the previous experiments with bubbles moving in a capillary (e.g., [6,7,16-27]) in the following aspect. In our experiments, the bubble/wall relative motion is created by translation of the wall, at fixed position of the bubble. Therefore, no pressure difference is required to induce the relative motion of the bubble and the wall. By using bubbles with diameter smaller than the internal diameter of the capillary, we ensure equal pressures in the aqueous phase on both sides of the wetting film (on the left-hand-side and on the right-hand-side of the immobile bubble), just as assumed in the theoretical consideration, Eq. (9), and as it is with 3D-films formed in the foam-wall experiments with actual foams. In contrast, the bubbles in the studies quoted above [6,7,16-27] were moving in capillaries under the action of a pressure difference applied on both sides of the bubble.

5.2. Experimental results and comparison with the theoretical model.

Typical microscope image of a dynamic 2D-wetting film formed between a bubble and the moving solid surface of a glass capillary, is shown in Fig. 3A. Four different regions in the profile of the bubble surface could be distinguished: (1) Region 1 at the entrance of the wetting film, in which the thickness of the liquid layer decreases down to the thickness of the subsequent flat (plateau) region 2. Due to the viscous friction, the radius of surface curvature in Region 1 is larger than the radius of curvature of the bubble surface at immobile solid wall; (2) Region 2, called also “the plateau region”, in which the film thickness remains almost constant. The thickness of the dynamic film in this region is significantly larger than the thickness of the equilibrium film at immobile wall. (3) Region 3, which is close to the exit of the film and where the liquid layer thickness sharply decreases. (4) Region 4, in which the layer thickness rapidly increases to merge with the meniscus region away from the film. The thinnest portion of the liquid layer (the constriction) is between regions 3 and 4. In a certain range of capillary numbers, one could discern a slight thickening of the film between regions 2 and 3, just before the constriction. This formation, called “bulge” in the literature [9], was relatively small in our experiments and, therefore, was not included explicitly in the theoretical model. On the other hand, the observed bulge demonstrates that the dynamic

pressure is highest between Regions 2 and 3, and this circumstance was used in the formulation of the model for the curved film profile. The observed regions resemble those calculated theoretically by Bretherton [18] - a comparison of the experimental results with the predictions of the Bretherton's model will be presented separately [35].

The shape of the bubble surface, as reconstructed from microscope images taken at different velocities of the capillary, V_0, are compared in Fig. 12A. Several trends can be noticed upon increase of V_0: First, the layer thickness increases everywhere. Second, the fraction of the bubble surface occupied by the flat region gradually decreases and disappears eventually at high velocities. Third, the radius of curvature in the first region (at the film entrance) and the area occupied by the transition zone film-meniscus (Region 1) gradually increase with V_0. In contrast, the radius of curvature and the width of the thin region at the film exit (Regions 3 and 4) do not change so significantly.

From the reconstructed film profiles, like those shown in Fig. 12A, one can determine the minimum layer thickness, which corresponds to h_2 in the curved film profile, as well the film thickness in the flat region (when it exists), which corresponds to h_1 in the theoretical model. Furthermore, one can determine from the experimental profiles the "harmonic mean" film thickness, defined by the expression:

$$\left(h_{harm}\right)^{-1} = \frac{1}{L}\int_0^L \frac{dx}{h} \tag{38}$$

which can be also compared to the theoretically predicted value of h_{harm}.

The experimental results for h_1, h_2, and h_{harm}, for surfactant solutions with and without glycerol are plotted in Fig. 12B, as a function of the capillary number, *Ca*. The symbols in Fig. 12B are experimental data, whereas the lines are theoretical predictions without any adjustable parameter (to account for the fact that the actual bubbles in the performed experiments were spherical, the capillary pressure in these calculations was set to $P_C = 2\sigma/R_B$). One sees that the agreement between the experimental points and the theoretical lines is very reasonable. Note that the power law index for the lines describing h_1 and h_2 were very similar (≈ 0.63), whereas the power law index for h_{harm} was significantly lower (≈ 0.47). The reasons for the different slopes of the lines describing $h_{1,2}$ and h_{harm}, as well as the relation between the friction force and h_{harm} will be further discussed in a separate study [35], after presenting a complete set of experimental data for mobile and immobile bubble surfaces.

The good agreement between the experimental results for the film thickness and the theoretical predictions is an indication that the model presented in Sections 2-3 describes adequately the systems under investigation, despite the fact that the actual shape of the bubble surface is represented by approximate model functions (see also Figs. 13 and 14 discussed in the following Section 6).

6. Discussion and comparison with some literature results.

In this section we compare the theoretical predictions for the friction force, F_{FR}, with experimental data from literature [7] and with theoretical calculations of other authors [9,18]. Then we discus briefly the scaling of F_{FR} with the capillary number, Ca.

To check how the predictions of the current model comply with experimental data for the friction of bubbles with solid wall (beside the comparison with our own data discussed in Section 3.3.1 of Ref. [11]), we analyzed the recent experimental results by Terriac et al. [7]. These authors [7] measured the velocity of train of bubbles moving along a capillary tube under an applied driving pressure. From the driving pressure, one can calculate the friction force, F_{FR}. The authors of Ref. [7] provide also the length of the bubbles, L, and the radius of curvature of the Plateau borders, R_P, from which one can calculate the length of the formed 2D-wetting films between the bubbles and the tube wall, $2R_F$. Thus a direct comparison of the experimental data from [7] with the current theoretical model is possible. This comparison evidenced a very good agreement (within 10 %) for all experimental data without using any adjustable parameter. For illustration, we show in Fig. 13 the theoretical curves and the experimental data from Ref. [7] for two sets of experiments, corresponding to different ratios R_F/R_P (the other experimental data are described equally well by the model). The observed "effective" power-low index in these measurements, $n \approx 0.56 \pm 0.02$ [7], thus appears as a combination of the indexes characterizing the friction in the film and in the transition region film-meniscus, $n = 1/2$ and $n \approx 2/3$, respectively (cf. Eq. (25')).

To check further our theoretical approach, we performed numerical calculations for tangentially mobile surface of the bubbles by changing the boundary condition, Eq. (8), to ensure stress-free bubble surface, viz. the condition $(\partial V_x/\partial z) = 0$ at $z = h$ was used. A linear model profile (the simplest possible, Fig. 2) was used for the fluid surface of the wetting film. The capillary pressure was defined as $P_C = 2\sigma/R_P$ in these calculations to adapt the theoretical model to the case of a single bubble moving in a capillary and to make a comparison of the model predictions with the Bretherton's equation [18,38] and with the numerical simulations of Saugey et al. [9], see Fig. 14A. A very good agreement was found between the three models in the range of capillary numbers, $10^{-5} < Ca < 10^{-2}$. Note that Saugey et al. [9] did not use a model profile in their calculations, which evidences that the model profiles used in our approach do not affect strongly the final results for F_{FR}, unless very high capillary numbers and low volume fractions are used (see also Fig. 4C).

Probably, the most surprising prediction of the current model is that the friction in the transition region film-meniscus should not scale with $Ca^{2/3}$ at low capillary numbers. Indeed, the numerical results shown in Fig. 14B and Eq. (25) both predict $F_{FR} \propto Ca^{3/4}$ at low values, $Ca < 10^{-6}$. One of the difficulties in testing this theoretical prediction is that the thickness of the dynamic films becomes comparable to the range of the repulsive surface forces (stabilizing the film [42,43]) at very low velocities, so that the film thickness, $h \approx$ constant, and F_{FR} becomes proportional to Ca^1 in this regime [9]. Still, some hints that a flow regime

with $F_{FR} \propto Ca^{3/4}$ could be observed experimentally are found in the literature. Recently Dollet et al [8] observed that the viscous force imposed by a 2D-bubble raft on solid wall scales with the solution viscosity of power $n = 0.77 \pm 0.05$. These experiments were made at relatively low velocity of the bubbles, small ratio (R_F/R_P), and with relatively large bubbles, which are the conditions, at which our model predicts a scaling with $n \approx 3/4$. The data presented in Ref. [8] do not allow one to make a direct comparison of the experimental results with the model, but a more detailed analysis of these experimental data would be definitely of interest.

We cannot rule out completely the possibility that the obtained scaling of the friction in the transition region film-meniscus (the second and third terms in Eq. (25)) is affected to some extend by the chosen model profiles. However, the good agreement of the model predictions with several sets of experimental data (Figs. 12B and 13, and Ref. [11]) and with the theoretical results by other authors (Fig. 14A) show that our model is able to describe quantitatively the bubble-wall friction force (despite its deviation from the Bretherton's scaling law at small values of Ca). It is worthwhile noting that several assumptions are used in the derivation of the Bretherton's law, $Ca^{2/3}$, which are not applicable to the systems under consideration in the current study. For example, such assumptions are: (1) The bubble shape in the transition region does not depend on the film length, and (2) There is a plug liquid flow inside the central zone of the film [18]. Therefore, the Bretherton model, as defined, corresponds to different flow regime in the dynamic film, so that one should not expect this model to be strictly applicable to the systems considered here (though it could be a reasonable approximation in a certain range of capillary numbers and volume fractions). Therefore, the scaling with $Ca^{3/4}$ predicted by the current model at low capillary numbers deserves further investigation, despite its contradiction to the scaling with $Ca^{2/3}$ predicted by Bretherton's model [18].

Furthermore, it is known for decades that the Bretherton's model fails to predict the friction force and the film thickness in many experiments with bubbles/drops moving in capillaries [7,16-19,21]. The most probable reason for the observed discrepancy is the possible effect of surfactants (or even traces of them, which easily appear as contaminations) on the surface mobility of the bubbles [25,26,44,45]. In many cases, a scaling with $Ca^{1/2}$ was observed experimentally [16-19,21,22], which corresponds to the predictions of the current model in the case of film-dominated viscous friction. Theoretical study is under a way to classify the various possible flow regimes in the bubble-wall friction zone (immobile vs. immobile surfaces, partial surface mobility, long and short bubbles, etc.) and to clarify the relation between the actual experimental conditions, the flow regime in the liquid layer, and the scaling laws for the friction force and film thickness.

7. Conclusions.

The major aim of this study is to explore theoretically how the friction between a single bubble and a smooth solid wall depends on the relative size of the wetting film, R_F/R_P, for bubbles with tangentially immobile surfaces. By using the lubrication approximation we show that:

1. Both the wetting film and the transition zones film-meniscus contribute into the total friction force. The latter is presented as a superposition of two components, which scale differently with the capillary number, Ca: the friction inside the film scales as $Ca^{1/2}$, whereas the friction in the meniscus region scales approximately as $Ca^{2/3}$, see Eq. (25'). As a result, the relative contribution of the meniscus region into the friction force increases with the value of Ca.

2. At high air volume fraction, $\Phi > 0.99$ and $\Phi_{3D} > 0.95$, the friction in the wetting film prevails at arbitrary values of $Ca < 0.1$. However, at moderate and low air volume fractions, the friction in the meniscus region could be comparable to that in the film, Fig. 5.

3. Simple explicit expressions were found to describe very well the numerical results for the friction force, Eq. (25), and the thickness of the wetting film, Eqs. (26) and (27), in a wide range of capillary numbers and air volume fractions. The predicted deviations from the Bretherton scaling law, $Ca^{2/3}$, at high and low capillary numbers, are discussed in Section 6.

4. Observations with optical microscope show that the dynamic wetting films between the bubbles and moving solid wall have complex shape with several distinct regions, Fig. 3. This shape is implemented in the curved model profile of the bubble surface, used in the numerical calculations. The measured film thickness agrees very well with the theoretical predictions without any adjustable parameter, Fig. 12B.

5. The theoretical approach is verified by comparing its predictions with the results of other authors [7,9,18] for the bubble-wall friction force, Figs. 13 and 14.

Acknowledgements. This study was funded by Unilever R&D, Trumbull, USA, and by the Bulgarian National Science Fund (Project "University research center for nanotechnologies and new materials"). The authors are grateful to Dr. A. Kraynik (Sandia Laboratory) for giving the idea for the experiment described in Section 5, and to Prof. I. B. Ivanov for the helpful discussions. The authors of Refs. [7,9,10] are gratefully acknowledged for sending preprints of their papers prior to publication. This work was first presented at the FRIT workshop organized by Prof. S. J. Cox in Aberystwyth, UK (27-28 June, 2005; http://users.aber.ac.uk/sxc/frit/html).

References

1. A.M. Kraynik, Ann. Rev. Fluid Mech. 20 (1988) 325.
2. Yoshimura, R. K. Prud'homme, J. Rheology 32 (1988) 53
3. H.M. Princen, J. Colloid Interface Sci. 105 (1985) 150.
4. H.M. Princen, A.D. Kiss, J. Colloid Interface Sci. 128 (1989) 176.
5. H.M. Princen, in: J. Sjöblom (Ed.), Encyclopedia of Emulsion Technology, Marcel Dekker, New York, 2001, Chapter 11, p. 243.
6. I. Cantat, N. Kern, R. Delannay, Europhys. Lett. 65 (2004) 726.
7. E. Terriac, J. Etrillard, I. Cantat, Europhys. Lett. (2006) in press.
8. B. Dollet, F. Elias, C. Quilliet, A. Huillier, M. Aubouy, F. Graner, Colloids & Surfaces A 263 (2005) 101.
9. Saugey, W. Drenkhan, D. Weaire, Phys. Fluids (2006) in press.
10. R. Höhler, S. Cohen-Addad, J. Phys. C: Condens. Matter 17 (2005) 1041.
11. N. D. Denkov, V. Subraminian, D. Gurovich, A. Lips, Colloids & Surfaces A 263 (2005) 129.
12. L. Becu, P. Grondin, A. Colin, S. Manneville, Colloids & Surfaces A 263 (2005) 146.
13. S.P. Meeker, R.T. Bonnecaze, M. Cloitre, Phys. Rev. Lett. 92 (2004) 198302-1.
14. S.P. Meeker, R.T. Bonnecaze, M. Cloitre, J. Rheol. 48 (2004) 1295.
15. U. Seifert, Phys. Rev. Lett. 83 (1999) 876.
16. F. Fairbrother, A. E. Stubbs, J. Chem. Soc. 1 (1935) 527.
17. G. I. Taylor, J. Fluid Mech. 10 (1961) 161.
18. F.P. Bretherton, J. Fluid Mech. 10 (1961) 166.
19. H.L. Goldsmith, S.G. Mason, J. Colloid Sci. 18 (1963) 237.
20. G.J. Hirasaki, J.B. Lawson, Soc. Petroleum Eng. J. 25 (1985) 176.
21. L.W. Schwartz, H.M. Princen, A.D. Kiss, J. Fluid Mech. 172 (1986) 259.
22. J.-D. Chen, J. Colloid Interface Sci. 109 (1986) 341.
23. J. Ratulowski, H.C. Chang, J. Fluid Mech. 210 (1990) 303.
24. K.G. Kornev, A.V. Neimark, A.N. Rozhkov, Adv. Colloid Interface Sci. 82 (1999) 127.
25. K.J. Stebe, S.-Y. Lin, C. Maldarelli, Phys. Fluids A 3 (1991) 3.
26. K.J. Stebe, C. Maldarelli, J. Colloid Interface Sci. 163 (1994) 177.
27. W. Drenkhan, S.J. Cox, G. Delaney, H. Holste, D. Weaire, N. Kern, Colloids Surfaces A 263 (2005) 52.

28. T. Cubaud, C.-M. Ho, Physics Fluids 16 (2004) 4575.

29. H.A. Stone, A.D. Stroock, A. Ajdari, Annu. Rev. Fluid Mech. 36 (2004) 381.

30. J. M. Gordillo, Z. Cheng, A.M. Ganan-Calvo, M. Márquez, D.A. Weitz, Phys. Fluids 16 (2004) 2828.

31. C.N. Baroud, H. Willaime, Compt. Rendus Physique 5 (2004) 547.

32. H.M. Princen, Langmuir 2 (1986) 519.

33. H.M. Princen, A.D. Kiss, Langmuir 3 (1987) 36.

34. A.D. Roberts, D. Tabor, Proc. R. Soc. Lond. A. 325 (1971) 323.

35. K. Golemanov, S. Tcholakova, N. Denkov, V. Subramanian, A. Lips, manuscript in preparation.

36. B.N.J. Persson, Sliding Friction: Physical Principles and Applications, Springer, Berlin, 1998, Chapter 7, p. 98.

37. Another closure for the system of equations was suggested by Terriac et al. [7], who set equal the force exerted on the wall and the dissipated energy inside the liquid layer. We checked analytically that, at least for the system under consideration here, the respective integrals are identical so that we could not use the closure suggested in [7].

38. Various numerical factors are quoted in the literature for the friction force in the Bretherton's model [18]. Considering tangentially mobile surface of the bubbles, Breteherton calculated 3.58 as a prefactor for the dynamic pressure drop created by the friction at the front edge of the bubble, and 0.93 for the friction at the rear edge. Summing these up, he found that the total pressure drop should be 4.52, see p. 172 in [18]. However, in his abstract (p. 166 in [18]) he quoted only the coefficient for the leading meniscus. As a result, various authors cite either the total value [11,26] or the value for the leading meniscus only [7,24]. The numerical factor of Bretherton is usually further multiplied by $3^{2/3}$ to transform the final result in terms of Ca (instead of $3Ca$, as in [18]). For $h/R_P << 1$, the friction force in Bretherton's model can be estimated as (dynamic pressure drop $\times \pi R_P^2 / 2\pi R_P$). Using the total dynamic pressure drop, for mobile bubble surface we thus obtain a numerical coefficient $4.52 \times 3^{2/3} = 4.70$, as quoted in Eq. (2.45) in [11]. For immobile surfaces, one can follow the approach in Section 3.2 of [18] to obtain that the numerical coefficient should increase by a factor of $2^{2/3}$ for tangentially immobile meniscus regions, which gives 7.46 as discussed in the paragraph after Eq. (25') of this study.

39. R. Delannay, I. Cantat, J. Etrillard, presentation at the 5th Eurofoam conference on Foams, Emulsions and Applications, Champs-sur-Marne, France, 5-8 July, 2004.

40. H.C. Cheng, R. Lemlich, Ind. Eng. Chem. Fundam., 22 (1983) 105.

41. M. Borne, E. Wolfe, Principles of Optics; 6th ed.; Pergamon Press: Oxford, 1980.

42. I. B. Ivanov Ed., Thin Liquid Films: Fundamentals and Applications; Marcel Dekker: New York, 1988.

43. J.N. Israelachvili, Intermolecular and Surface Forces, 2nd ed.; Academic Press: New York, 1992.
44. I.B Ivanov, D.S. Dimitrov. Thin film drainage. In: Thin Liquid Films: Fundamentals and Applications. Ed. Ivanov, I. B.; Marcel Dekker: New York, 1988, Chapter 7.
45. I. B. Ivanov, Pure Applied Chem. 52 (1980) 1241.

Appendix

Approximate expression for F_{FR} (linear profile).

Here we explain how the approximate expressions for the friction force, F_{FR}, such as Eq. (25), were designed. At high air volume fractions, the ratio $(R_F/R_P) > 3$ and the friction in the film dominates (see Fig. 5A), so that the friction terms for the meniscus regions, $F_{FR}^{(1)}$ and $F_{FR}^{(3)}$ in Eq. (24), can be neglected. At low air volume fractions, $(R_F/R_P) < 1$ and the parameters $\delta_{1,2}$ in Eq. (24) are small, $\delta_{1,2} << 1$. In this case, one can expand Eqs. (24a) and (24c) in series to evaluate the main terms for the friction force in the meniscus regions. The result can be expressed in the form of an infinite series:

$$\frac{F_{FR}^{(1)}+F_{FR}^{(2)}+F_{FR}^{(3)}}{\sigma}=A_{Film}\left(Ca\frac{R_F}{R_P}\right)^{1/2}+Ca\left(\sum_{m=0}^{\infty}A_m\left(Ca\frac{R_F}{R_P}\right)^{(m-1)/4}\right) \tag{A.1}$$

where the first term accounts for the friction in the film, whereas the remaining infinite series accounts for the friction in the two meniscus regions. The multipliers A_{Film} and A_m in Eq. (A.1) are of the order of unity. The leading four terms for the friction in the meniscus region are:

$$\frac{F_{FR}^{(1)}+F_{FR}^{(3)}}{\sigma}=Ca\left(\begin{array}{l}\left(Ca\frac{R_F}{R_P}\right)^{-1/4}\frac{2\pi}{2\sqrt{2}}\left(\frac{4\eta_1-3\tilde{Q}}{\eta_1^{3/2}}+\frac{4\eta_2-3\tilde{Q}}{\eta_2^{3/2}}\right)-(4\pi+8)+\\ \left(Ca\frac{R_F}{R_P}\right)^{1/4}\frac{3\pi}{4\sqrt{2}}\left(\frac{4\eta_1+3\tilde{Q}}{\eta_1^{1/2}}+\frac{4\eta_2+3\tilde{Q}}{\eta_2^{1/2}}\right)-\\ \left(Ca\frac{R_F}{R_P}\right)^{1/2}\frac{4}{3}\left(3\tilde{Q}+\eta_1+\eta_2\right)+O\left[\left(CaR_F/R_P\right)^{3/4}\right]\end{array}\right) \tag{A.2}$$

Eq. (A.2) shows that the two leading terms for the friction inside the meniscus region are proportional to $Ca^{3/4}$ and Ca, respectively (we recall that Ca <<1 in the entire consideration). Note, however, that the parameters entering A_m, such as $\eta_{1,2}$ and $\tilde{Q}$, also depend on Ca in a complex way (though this dependence is relatively weak, except at very low volume fractions - see Fig. 8). That is why, to find an explicit approximate expression for the friction force, we fitted the numerical data for the friction force in the meniscus region by a function containing only the leading powers of Ca, and by considering the multipliers A_m as free parameters. The fit by the least-squares method showed that the following interpolating formula describes rather well the numerical results:

$$F_{FR} \approx 2.56 Ca^{1/2} \sigma \left(\frac{R_F}{R_P} \right)^{1/2} + 4 \left(\frac{R_P}{R_F} \right)^{1/4} \left(2Ca^{3/4} - 3Ca \right) \qquad \text{(linear profile)} \quad \text{(A.3)}$$

where the first term accounts for the friction in the film (cf. with the result for linear profile in Ref. [11]), whereas the remaining terms account for the friction in the meniscus region.

Explicit expressions for F_{FR} in the case of curved profile.

The integration of Eq. (22) gives the following expressions for the various components of the friction force in the case of curved film profile (Fig. 4B):

$$F_{FR} = F_{FR}^{(1)} + F_{FR}^{(2)} + F_{FR}^{(3)} + F_{FR}^{(4)} \qquad \text{(A.4)}$$

$$\frac{F_{FR}^{(1)}}{\sigma} = Ca \left(\begin{array}{l} \dfrac{\mathrm{ArcSin}\left(\dfrac{1}{1+\delta_{0C}} \right) - \mathrm{ArcSin}\left(\dfrac{\eta_0 \left(1+\delta_{0C}\right) - \eta_{0C}\left(2+\delta_{0C}\right)}{\eta_0} \right)}{\eta_{0C} \sqrt{\delta_{0C}\left(2+\delta_{0C}\right)}} \left(4\eta_{0C}\left(1+\delta_{0C}\right) - \dfrac{3\eta_1}{\left(2+\delta_{0C}\right)} \right) - \\ 4\mathrm{ArcSin}\left(\dfrac{\eta_{0C}\left(1+\delta_{0C}\right) - \eta_0 \delta_{0C}}{\eta_{0C}} \right) - \dfrac{3\eta_1}{\eta_{0c}\left(2+\delta_{0C}\right)} + \\ \dfrac{3\eta_1 \left(1+\delta_{0C}\right) \sqrt{\left(\eta_0 - \eta_{0C}\right)\left(2\eta_{0C}/\delta_{0C} - \eta_0 + \eta_{0C}\right)}}{\eta_0 \eta_{0c} \left(2+\delta_{0C}\right)} \end{array} \right)$$

$$\frac{F_{FR}^{(2)}}{\sigma} = \frac{2\sqrt{2} Ca^{3/4}}{\eta_1^{1/2}} \left(\frac{R_P}{R_F} \right)^{1/4} \frac{1}{m^{1/2}} \left(\frac{5}{4} \mathrm{ArcTan}\left(-\left(\frac{\eta_0}{\eta_1} - 1 \right)^{1/2} \right) + \frac{3}{4} \left(\frac{\eta_1}{\eta_0} \right)^{1/2} \left(1 - \frac{\eta_1}{\eta_0} \right)^{1/2} \right)$$

$$\frac{F_{FR}^{(3)}}{\sigma} = 2kCa^{1/2} \left(\frac{R_F}{R_P} \right)^{1/2} \frac{1}{\eta_1^{1/2} \eta_2^{1/2}} \left(\frac{5\eta_2 - 3\eta_1}{2\eta_2} \right)$$

$$\frac{F_{FR}^{(4)}}{\sigma} = 2Ca \left(\frac{\dfrac{\pi}{2} + \mathrm{ArcSin}\left(\dfrac{1}{1+\delta_2} \right)}{\eta_2 \sqrt{\left(1 + 2/\delta_2\right)}} \left(2\eta_2 + 2\frac{\eta_2}{\delta_2} - \frac{3\eta_1}{2\delta_2\left(2+\delta_2\right)} \right) - \pi - \frac{3\eta_1}{2\eta_2\left(2+\delta_2\right)} \right)$$

where by definition $s \equiv x_0/R_P$ and

$$\eta_0 = \eta_1 + \frac{1}{2} Ca^{-1/2} \left(\frac{R_P}{R_F} \right)^{1/2} \left(2R_F \left(1-k \right) / R_P + 1 - s \right) \frac{1-s}{\sqrt{2s-s^2}} \tag{A.5}$$

The terms $F_{FR}^{(1)}$ and $F_{FR}^{(4)}$ account for the friction in the two meniscus regions, whereas ($F_{FR}^{(2)}$ + $F_{FR}^{(3)}$) accounts for the friction inside the film. By lengthy but straightforward calculations one can show that the friction inside the film is proportional to $(CaR_F/R_P)^{1/2}$, whereas the leading terms for the friction inside the meniscus regions are proportional to $Ca^{3/4}$ and Ca. By applying a least-squares fit to the numerical results, we found that Eq. (25) describes adequately the friction force for the curved film profile.

Table 1. Air volume fractions for 2D- and 3D-foam bubbles, Φ and Φ_{3D}, corresponding to similar values of the dimensionless radius of the wetting film, $R_F/(R_F+ R_P)$, formed upon bubble contact with solid wall. The calculations are made using the Princen's formulas [5], Eqs. (1)-(3), (33),(34).

	Air volume fraction	
$R_F/(R_F + R_P)$	Φ	Φ_{3D}
0.1	0.925	0.733
0.2	0.940	0.773
0.4	0.965	0.872
0.5	0.977	0.913
0.6	0.985	0.945
0.8	0.996	0.986
0.9	0.999	0.996

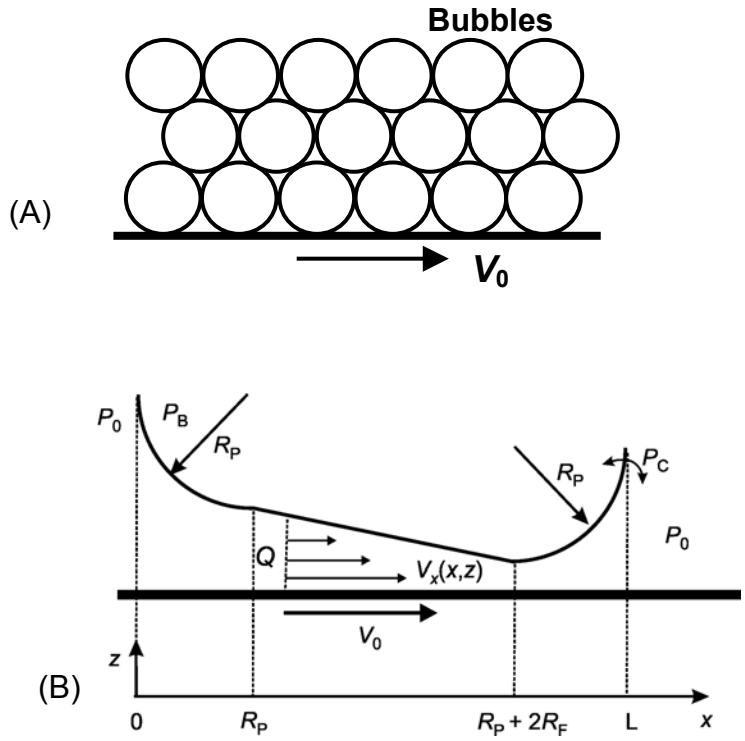

Fig. 1. Schematic presentation of the system under consideration: (A) Smooth solid substrate is moving with constant linear velocity, V_0, with respect to a plug of foam bubbles; (B) The liquid entrainment into the wetting film, formed between the bubble and the moving substrate, leads to an asymmetric film configuration with larger film thickness at the entrance region.

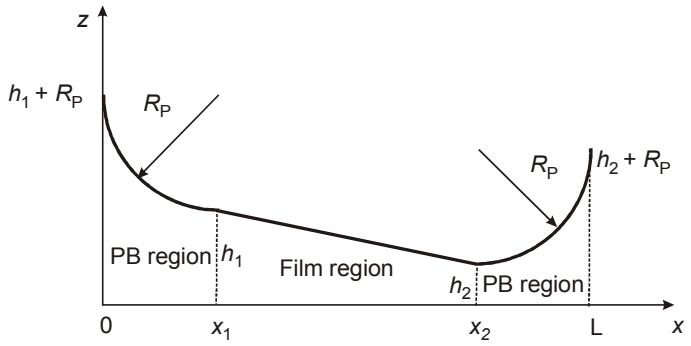

Fig. 2. Schematic presentation of one of the assumed model profiles for the bubble surface, linear upper surface of the wetting film, Eqs. (4a)-(4c).

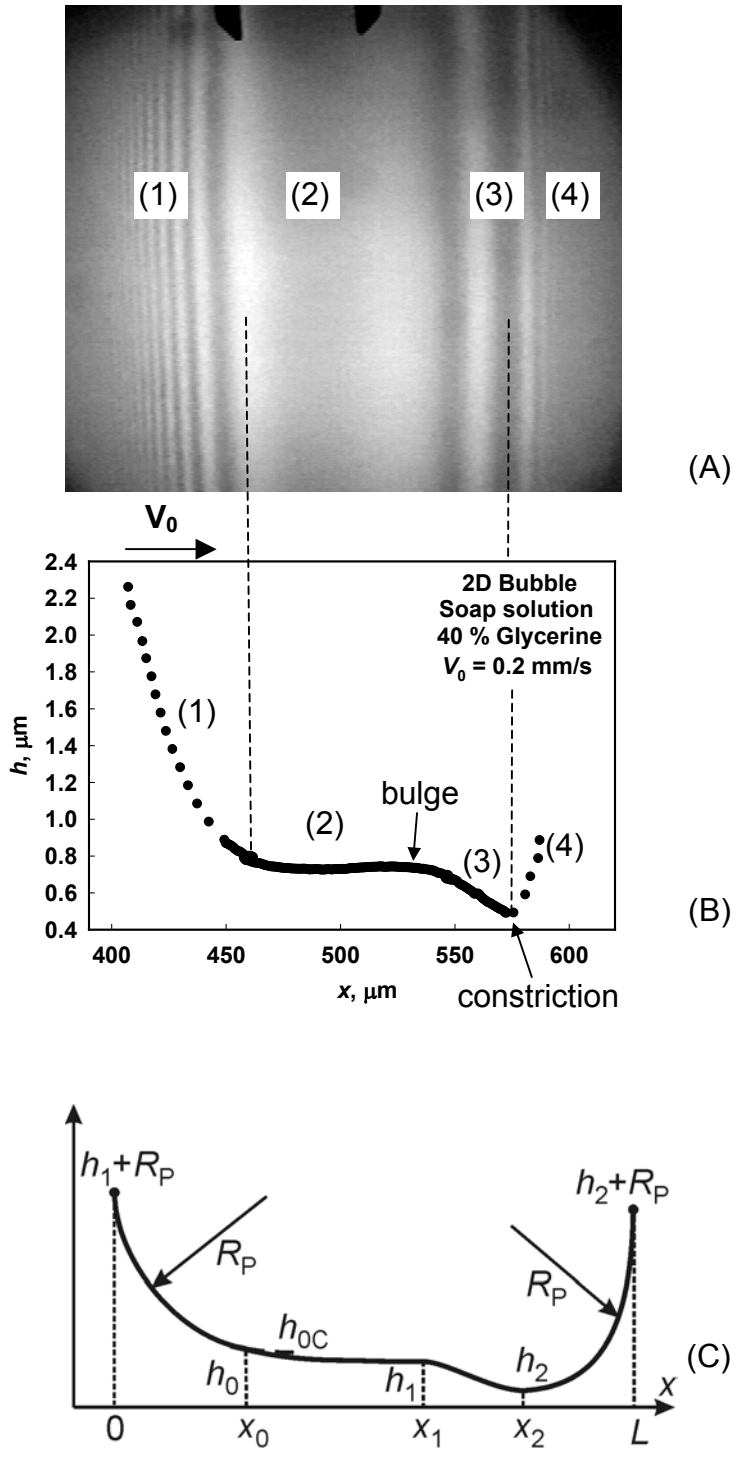

Fig. 3. (A) Photograph of the wetting film formed between a 2D-bubble and a solid wall, which moves with a linear velocity, V_0 = 0.2 mm/s; (B) Restored profile of the bubble surface in the zone of bubble-wall contact; the regions described in Section 5.2 are indicated by the integers 1-4; (C) Schematic presentation of the assumed curved model profile of the bubble surface, Eqs. (5a)-(5d).

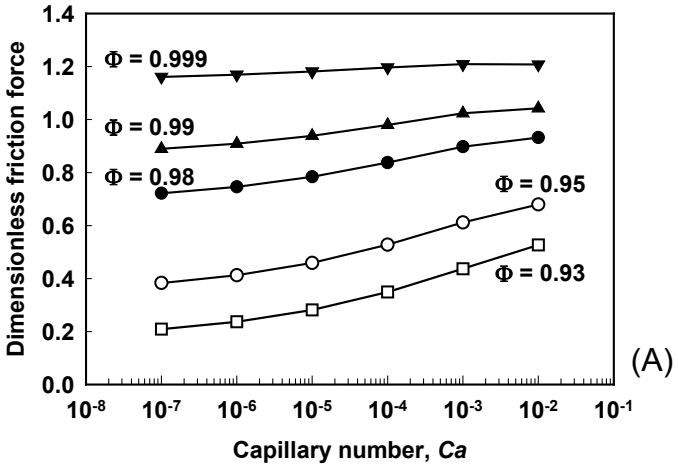

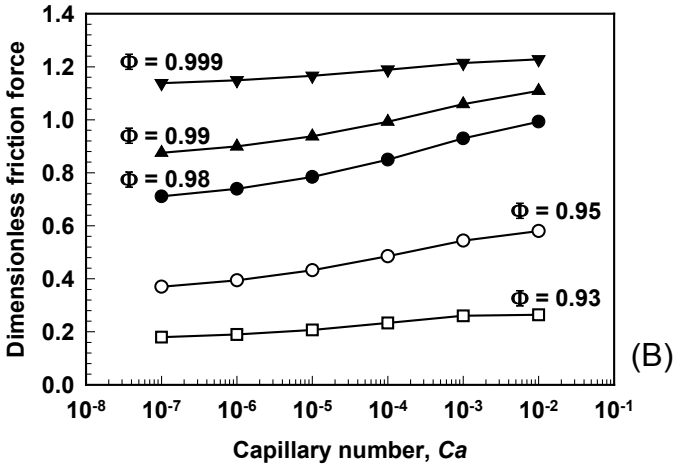

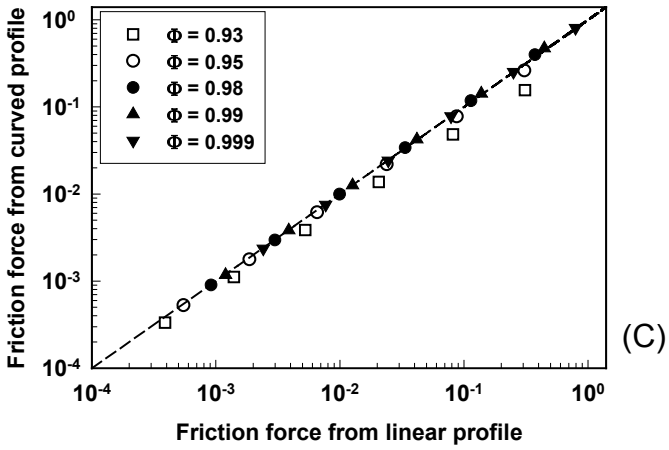

Fig. 4. Dimensionless friction force, calculated as a function of the capillary number, at different air volume fractions: (A) Linear film profile, (B) Curved film profile, (C) Correlation plot of the friction forces calculated with the two model profiles.

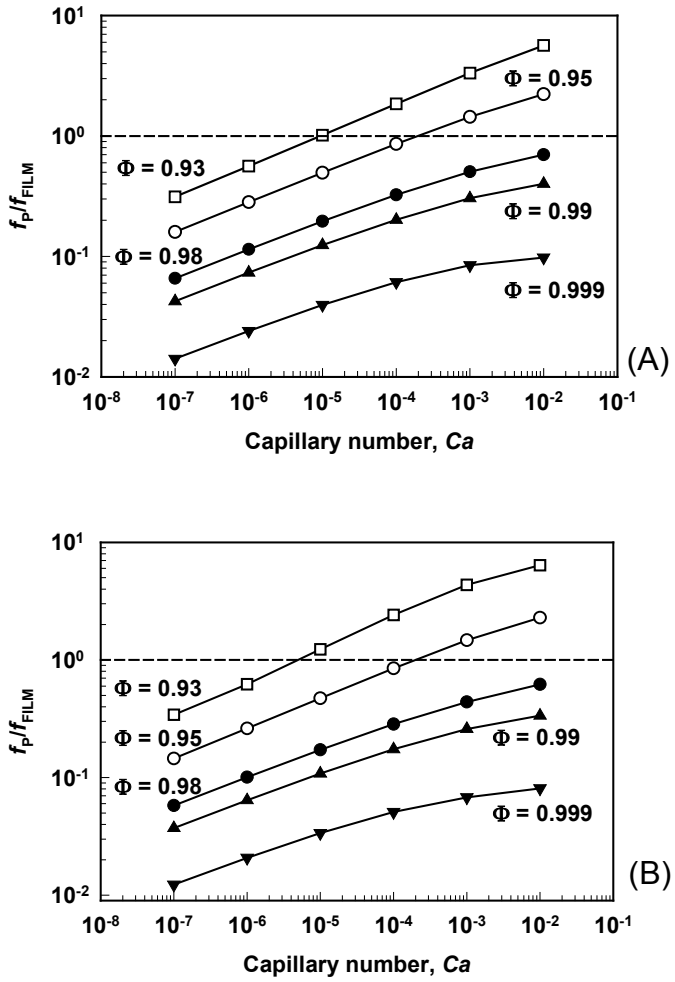

Fig. 5. Ratio of the friction force inside the meniscus region to the friction force inside the film region, as a function of the capillary number at different air volume fractions, as calculated with: (A) Linear profile, (B) Curved profile of the fluid film surface.

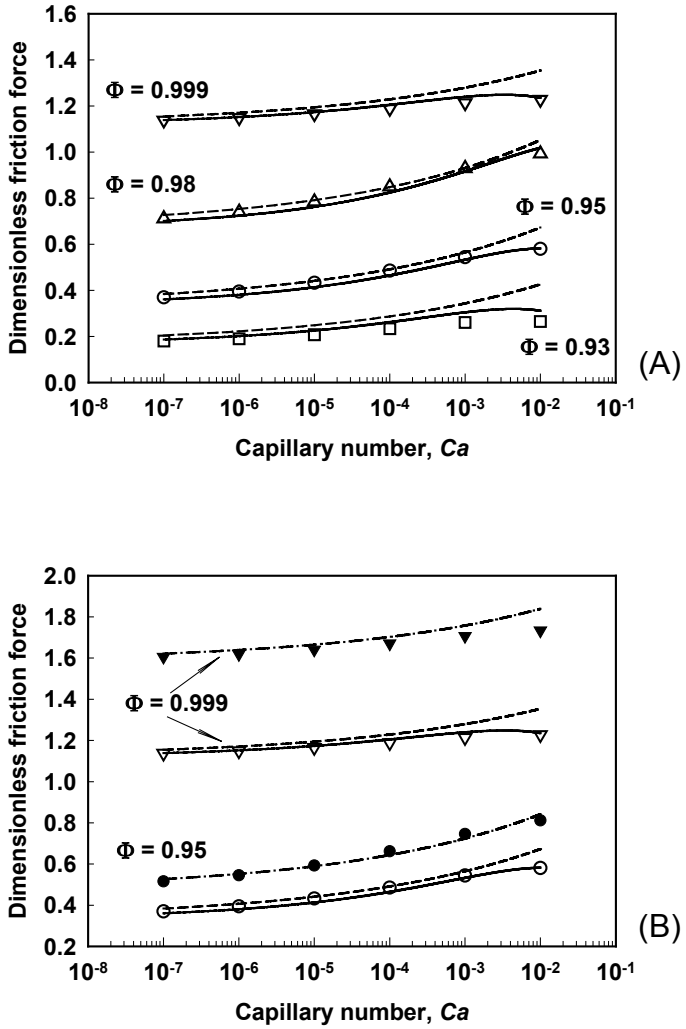

Fig. 6. Comparison of the numerically calculated dimensionless friction force, $\tilde{F}_{FR}$, as a function of the capillary number at different air volume fractions, Φ, with the explicit expressions: Eq. (25) – solid curves; Eq.(25') – dashed curves; Eq. (25") – dash-dotted curves. The numerical calculations (symbols) are made with the curved model profile: (A) Assuming $P_C = \sigma/R_P$. (B) The open symbols are calculated with $P_C = \sigma/R_P$, whereas the full symbols with $P_C = 2\sigma/R_P$.

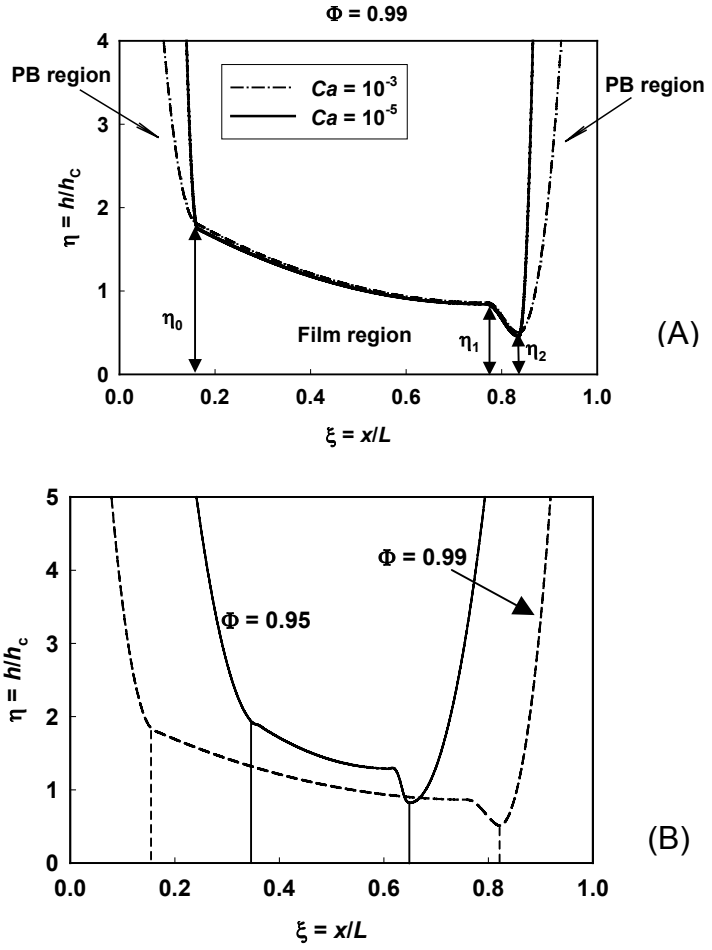

Fig. 7. (A) Dimensionless thickness of the liquid layer, $\eta = h/h_C$, as a function of the scaled x-coordinate, $\xi = x/L$, calculated at $Ca = 10^{-3}$ (dash-dot curve) and $Ca = 10^{-5}$ (solid curve) and $\Phi = 0.99$. (B) Dimensionless thickness, $\eta(\xi)$, calculated at $Ca = 10^{-3}$ and different air volume fractions, $\Phi = 0.95$ (solid curve) and $\Phi = 0.99$ (dashed curve). The calculations are made with curved profile of the bubble surface, Eqs. (5a)-(5d).

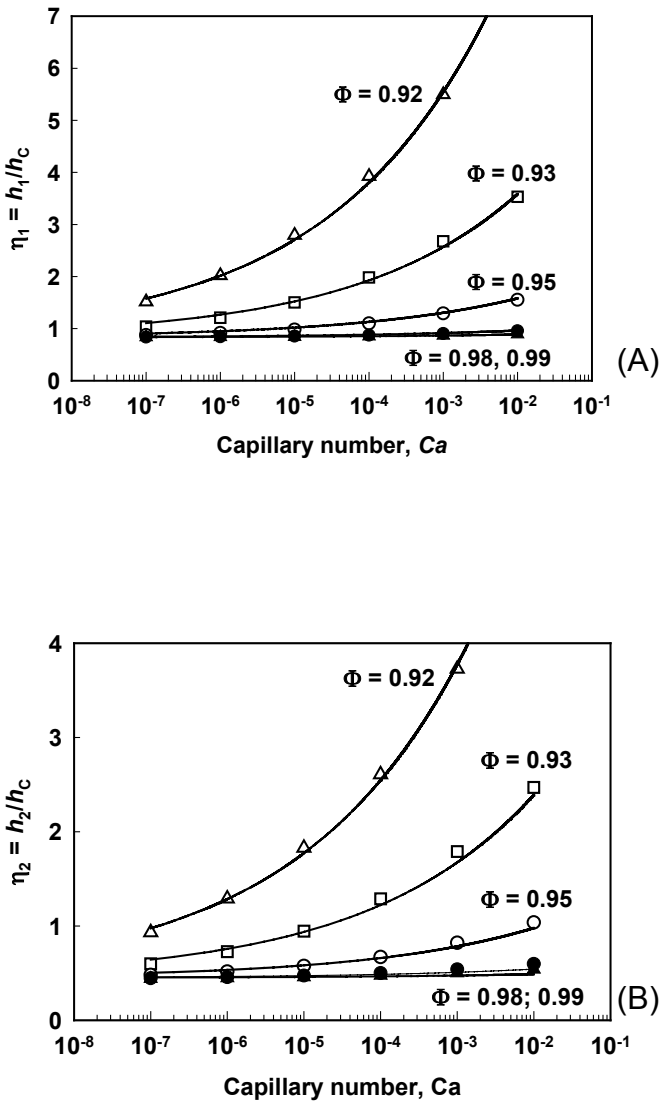

Fig. 8. Dimensionless layer thickness, calculated as a function of the capillary number with the curved profile of the bubble surface (the symbols), along with the interpolating empirical fits, Eqs. (26) and (27): (A) $\eta_1 = h_1/h_C$, and (B) $\eta_2 = h_2/h_C$. Φ is the air volume fraction.

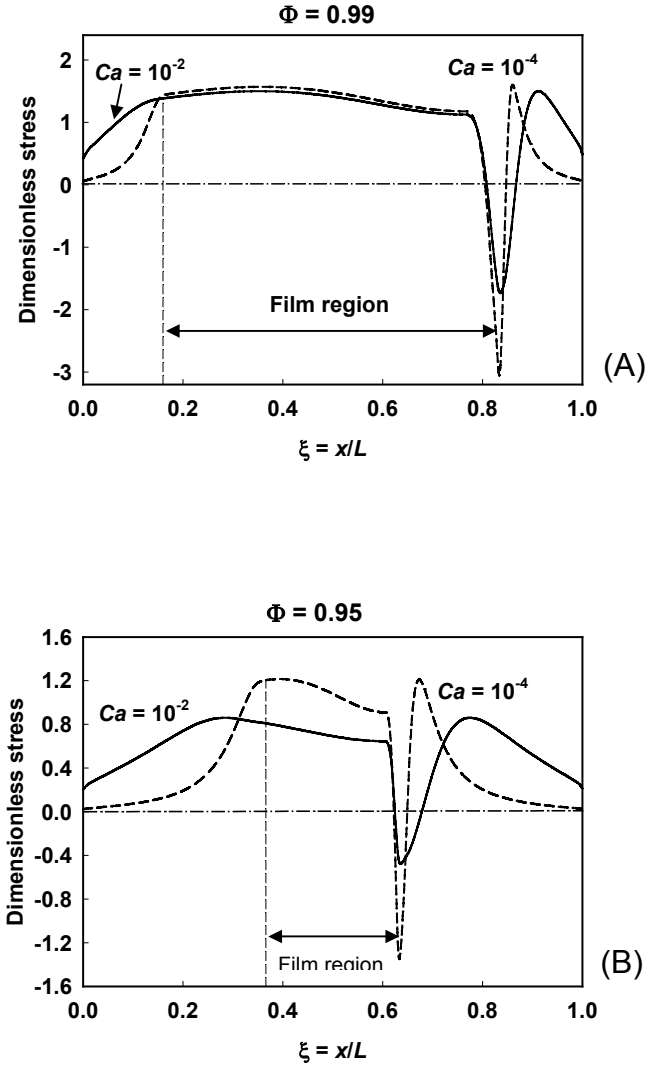

Fig. 9. Dimensionless viscous stress on the wall, $\tilde{\tau} = \tau R_F / P_C h_C^{1/2}$, as a function of the scaled lateral coordinate, $\xi = x/L$, calculated with the curved profile of the fluid film surface, at two capillary numbers: $Ca = 10^{-2}$ (continuous curves) and $Ca = 10^{-4}$ (dashed curves): (A) $\Phi = 0.99$, and (B) $\Phi = 0.95$.

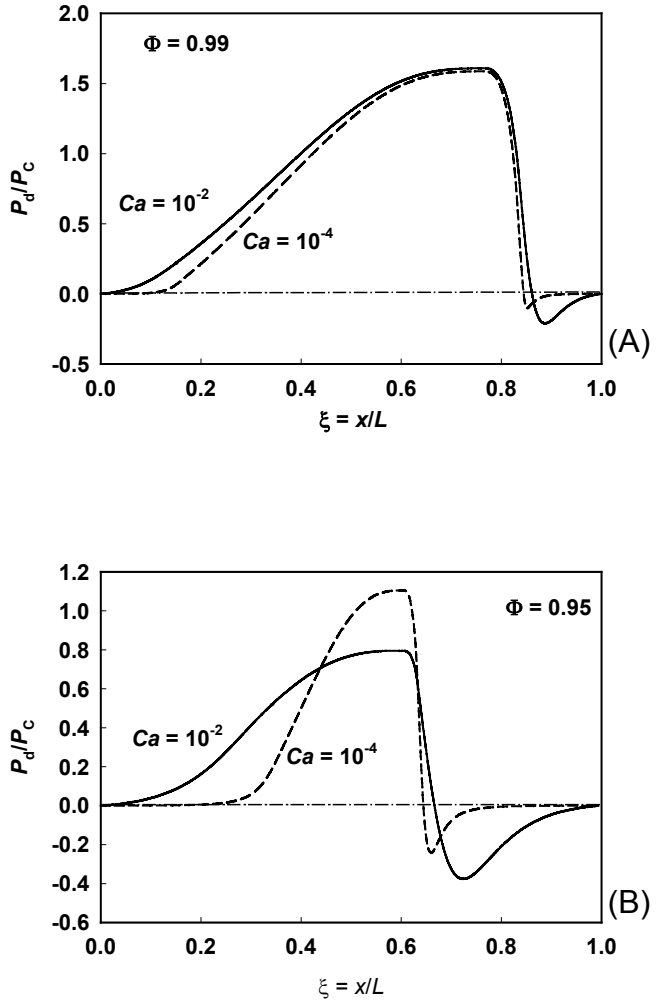

Fig. 10. Dimensionless dynamic pressure, $\tilde{P}_d = P_d\left(x\right)/P_C$, as a function of the scaled lateral coordinate, $\xi = x/L$, calculated with the curved profile of the fluid film surface at two capillary numbers, $Ca = 10^{-2}$ (continuous curves) and $Ca = 10^{-4}$ (dashed curves): (A) $\Phi = 0.99$, and (B) $\Phi = 0.95$.

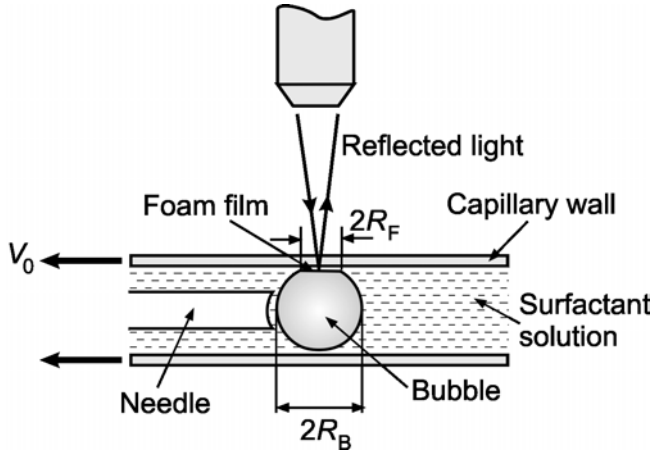

Fig. 11. Schematic presentation of the experimental setup used to observe the wetting film between a single bubble and the inner glass wall of a cylindrical capillary: The bubble is formed on the tip of a needle, which is placed in the glass capillary. The capillary is translated by motor with given velocity, V_0, and the wetting film between the bubble and the solid wall is observed by microscope, in reflected light. The film size, R_F, the bubble radius, R_B, and the film thickness, h, are determined as explained in the text.

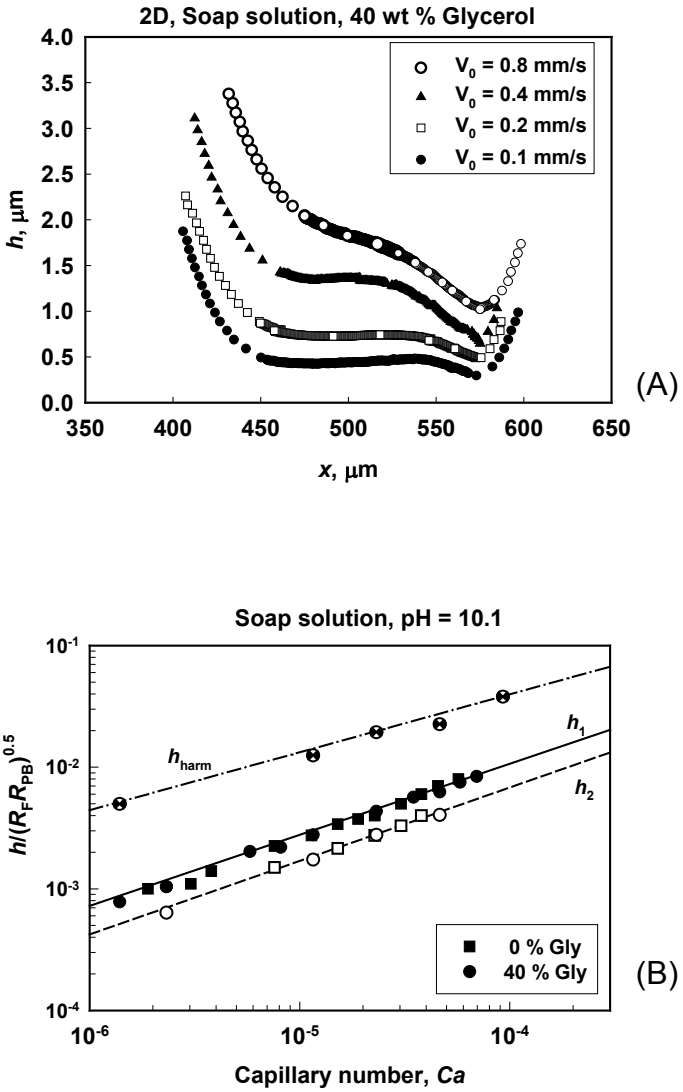

Fig. 12. Shape of the bubble surface and thickness of the liquid layer in the bubble-wall contact zone, for 2D-films formed as explained in Section 5 and Fig. 11. (A) Film thickness, h, as a function of the lateral coordinate, x, at different wall velocities, V_0. The bubble radius is ≈ 500 μm and the film radius is ≈ 75 μm. (B) Dimensionless film thickness in the flat film region, $h_1/(R_F R_P)^{1/2}$, at the constriction, $h_2/(R_F R_P)^{1/2}$, and the harmonic mean thickness, $h_{harm}/(R_F R_P)^{1/2}$ (see Eq. (38)) as functions of the capillary number.

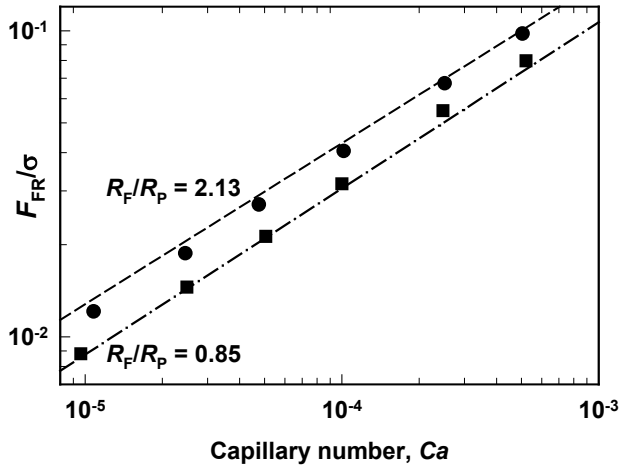

Fig. 13. Comparison of the theoretical predictions of the current model with experimental data from Ref. [7] without adjustable parameters. For clarity, only two sets of experimental data are shown, corresponding to $R_P/L = 0.16$ (the circles) and $R_P/L = 0.27$ (the squares) in the notation of Ref. [7].

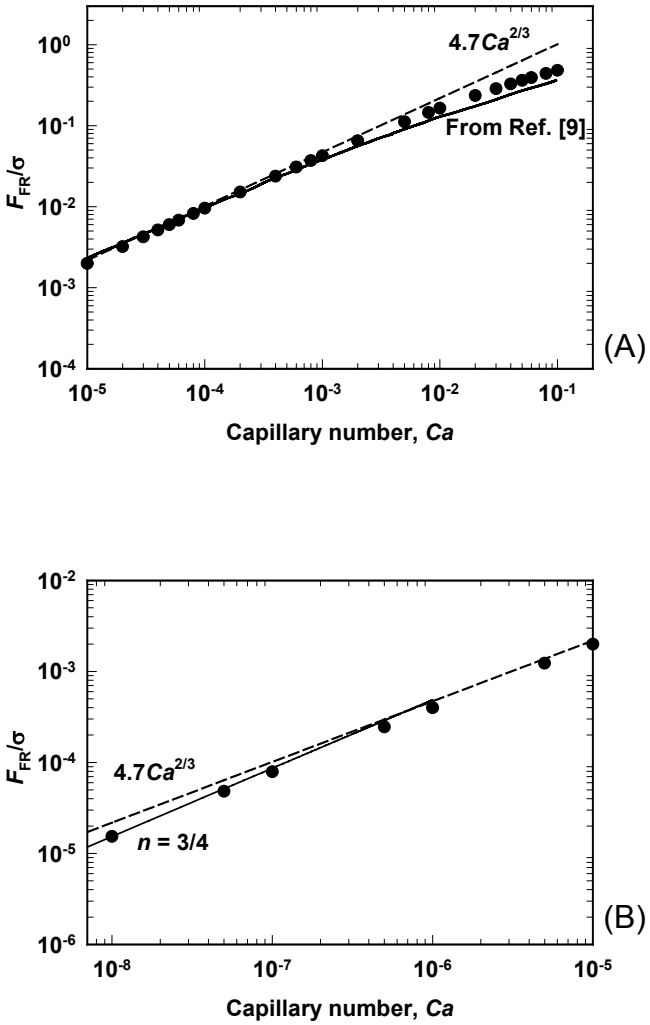

Fig. 14. Comparison of theoretically calculated friction forces between bubble with tangentially mobile surface and solid wall, according to the models of Bretherton [18] – dashed curve; Saugey et al. [9] – solid curve; and assuming linear profile of the film as in Fig. 2 – solid circles: (A) Intermediate and high capillary numbers, (B) Low capillary numbers.